

Deep Generative Modeling with Spatial and Network Images: An Explainable AI (XAI) Approach

Yeseul Jeon^{1,2}, Rajarshi Guhaniyogi¹, Aaron Scheffler²

¹Department of Statistics, Texas A&M University, College Station, TX, USA

²Department of Epidemiology & Biostatistics, University of California San Francisco, San Francisco, CA, USA.

Abstract

This article addresses the challenge of modeling the amplitude of spatially indexed low frequency fluctuations (ALFF) in resting state functional MRI as a function of cortical structural features and a multi-task coactivation network in the Adolescent Brain Cognitive Development (ABCD) Study. It proposes a generative model that integrates effects of spatially-varying inputs and a network-valued input using deep neural networks to capture complex non-linear and spatial associations with the output. The method models spatial smoothness, accounts for subject heterogeneity and complex associations between network and spatial images at different scales, enables accurate inference of each images effect on the output image, and allows prediction with uncertainty quantification via Monte Carlo dropout, contributing to one of the first Explainable AI (XAI) frameworks for heterogeneous imaging data. The model is highly scalable to high-resolution data without the heavy pre-processing or summarization often required by Bayesian methods. Empirical results demonstrate its strong performance compared to existing statistical and deep learning methods. We applied the XAI model to the ABCD data which revealed associations between cortical features and ALFF throughout the entire brain. Our model performed comparably to existing methods in predictive accuracy but provided superior uncertainty quantification and faster computation, demonstrating its effectiveness for

large-scale neuroimaging analysis. Open-source software in Python for XAI is available.

Keywords: Deep neural network; explainable artificial intelligence; Monte Carlo (MC) dropout; multimodal neuroimaging data; variational inference.

1 Introduction

Recently, a critical concern in the field of neuroimaging research has been unraveling the intricate relationships between images that capture different aspects of brain structures and function using magnetic resonance imaging (MRI). This involves integrating multimodal imaging data—specifically, (a) *brain network information* from functional MRI (fMRI), which quantifies connectivity between nodes, and (b) *brain spatial information* from structural MRI (sMRI) and fMRI, which provides ROI-level information. These data are often hierarchically structured, with ROIs nested within network nodes, offering insights at multiple spatial scales.

For example, this article is motivated by the challenge of modeling the amplitude of spatially indexed low-frequency fluctuations (ALFF) in resting state functional MRI (rs-fMRI) as a function of cortical structural features measured via sMRI and a multi-task coactivation network capturing coordinated patterns of brain activation measured via task-based fMRI (t-fMRI) in a large neuroimaging study of adolescents. Recent studies in computational and cognitive neuroscience suggest that ALFF serves as an indicator of brain functional integrity and supports information processing [Fu et al., 2017]. It has been linked to atypical cognitive development, cognitive decline, and various psychiatric disorders, highlighting its relevance for both basic and clinical neuroscience research [Sheng et al., 2021]. What remains unclear from current research is how spatial and network features of the brain contribute jointly to explain variability in ALFF. A major challenge in bridging this gap is a lack of available methods that can accommodate heterogeneity in multi-modal imaging data structures and the immense data volume produced in large neuroimaging studies while simultaneously providing principled inference.

The primary scientific objectives of this study encompass whole-brain analysis and are threefold: (a) to predict the spatially indexed ALFF outcome using both cortical structural predictors and a brain network predictor; (b) to jointly model the spatially varying effects of

the structural predictors on ALFF through interpretable regression functions, enabling inference on the independent contributions of cortical features; and (c) to quantify uncertainty in model components and predictions, facilitating principled statistical inference. These scientific goals must be met while accommodating the massive data volume produced from large neuroimaging studies required to detect the often-subtle effects that link brain image features.

To achieve these goals, this article proposes a two-stage generative modeling framework for input and outcome images. In the first stage, each network edge is modeled as an interaction between latent vectors associated with the connected nodes, enabling the estimation of node-specific latent effects. In the second stage, we adopt a semi-parametric regression approach that incorporates additive contributions from both spatial and network predictors. Spatial effects are captured using spatially varying coefficient functions, while the influence of each network node is modeled as a nonlinear function of the latent effects estimated in the first stage.

These nonlinear functions are modeled using deep neural networks (DNNs) with a dropout architecture. To perform inference, we employ *Monte Carlo dropout* (MC dropout) architecture, leveraging its connection to variational approximations of deep Gaussian processes (GP). This allows us to predict the output image and to estimate the regression effects of spatial predictors and nonlinear node effects, all with quantified uncertainty, offering one of the first explainable AI methods in the context of heterogeneous image-on-image regression.

1.1 Novelty of the Proposed Approach

(1) Integration of multimodal data for image prediction. The proposed framework seamlessly integrates spatial and network images across multiple scales, leveraging their structural relationships through a flexible, multiscale modeling approach to enable predictive inference for an outcome image. Image-on-image regression involving both spatial and network inputs remains largely underexplored, making this one of the first principled methods to address the problem. **(2) Explainable inference.** Our approach supports both point estimation and uncertainty quantification for the effects of spatial predictors and network nodes, as well as for the predicted outcome image. This enables interpretable inference and positions our method

as one of the *first deep learning-based* frameworks to offer explainability in image-on-image regression. **(3) Computational efficiency.** The model is highly scalable, with computation growing linearly in both the sample size and the number of ROIs, opening the possibility for its future applications in much larger neuroimaging studies. **(4) State-of-the-art performance.** Empirical results demonstrate that XAI achieves competitive point estimates and predictions while substantially outperforming existing methods in uncertainty quantification.

1.2 Related Work

Image datasets represent high-dimensional, structured data characterized by complex dependency patterns. To model these intricacies, many studies have leveraged deep learning architectures capable of capturing nonlinear dependencies through multiple layers of parameterization [Tsuneki, 2022, Razzak et al., 2018]. Bayesian deep learning frameworks are especially attractive due to their ability to offer enhanced flexibility by offering inference within a coherent probabilistic model. Bayesian methods have recently gained traction in medical imaging, with applications spanning classification, segmentation, registration, denoising, and tumor growth prediction [Herzog et al., 2020, Zou et al., 2023, Prince et al., 2023, Jeon et al., 2024, Luo et al., 2020]. However, the literature on deep learning in the context of predictive inference of response images based on predictor images, popularly referred to as the image-on-image regression, is notably sparse.

Deep convolutional neural networks (CNNs) have been extensively applied in computer vision tasks for image prediction, owing to their ability to preserve spatial structure through convolutional layers. However, most CNN-based algorithms are tailored to specific tasks [Santhanam et al., 2017] and commonly rely on architectures such as Visual Geometry Group (VGG) networks and Residual Neural Networks (ResNet). These architectures can inadvertently incorporate irrelevant features, leading to biased predictions [Isola et al., 2017]. To address general-purpose image-to-image regression problems, the Recursively Branched Deconvolutional Network (RBDN) was introduced. This architecture constructs a composite feature map that is processed through multiple convolutional branches, each dedicated to a specific

task [Santhanam et al., 2017]. Despite its flexibility, RBDN requires input and output images to be of identical dimensions—a limitation for applications involving images of varying sizes.

Generative adversarial networks (GANs) have been used for image-to-image regression, bypassing the lack of a standardized objective function by using adversarial training to improve image predictions [Isola et al., 2017]. However, standard GANs struggle to establish a direct link between input and predicted images [Huang et al., 2018], a limitation addressed by conditional GANs such as Pix2Pix, which produces sharper outputs. Some approaches combine GANs with discriminators like variational autoencoders (VAEs) to enhance performance. Nonetheless, GANs face challenges, including unstable training, difficulty in reaching equilibrium, and issues like vanishing gradients [Huang et al., 2018]. The absence of interpretable objective functions further limits their utility in scientific applications, such as in the prediction of variation in ALFF.

Aligned with our proposed framework, several recent studies have incorporated spatial information into Bayesian deep learning models [Kirkwood et al., 2022, Li et al., 2023, Zammit-Mangion et al., 2023, Mateu and Jalilian, 2022, Zhang et al., 2023a, Jeon et al., 2024]. For example, Mateu and Jalilian [2022] employed variational autoencoder-based generative networks to model spatio-temporal point processes, while Kirkwood et al. [2022] applied Bayesian deep neural networks for spatial interpolation. A growing line of work integrates deep learning with semiparametric regression to improve spatial modeling. Li et al. [2023] proposed a semiparametric approach where deep neural networks (DNNs) replace classical spline or kernel techniques to capture nonlinear spatial variation. Here, the parametric component captures spatial linear trends, while the DNN component flexibly models complex spatial dependencies using coordinates as inputs. Spatial Bayesian Neural Networks (SBNNs) [Zammit-Mangion et al., 2023] further extend Bayesian neural networks by introducing spatial embeddings and spatially varying parameters, enhancing modeling flexibility at the cost of increased computational burden due to high-dimensionality. Unlike our method, which efficiently captures spatially varying coefficients, SBNNs rely on spatial basis functions to learn weight and bias parameters through embedding layers.

A key challenge in our study of predicting ALFF using spatial and brain network images using deep learning approaches is interpretability, which involves drawing inference on regression effects of input images and quantifying predictive uncertainty for the output image. For interpretable machine learning in the context of image-on-image regression, one of the most relevant methods is BIRD-GP [Ma et al., 2023]—a two-stage Bayesian model that employs a combination of Gaussian processes (GPs) and deep neural networks. Specifically, this approach uses neural networks to learn basis expansions of input and output images, followed by nonlinear regression on vectorized projections of the input and output images. While BIRD-GP enhances interpretability and provides predictive uncertainty through the posterior distribution, its two-stage design involves estimating a large number of parameters, particularly for high-dimensional images. This leads to increased computational cost and a greater risk of overfitting.

The remainder of the paper is structured as follows. Section 2 describes the ABCD neuroimaging dataset and outlines the associated scientific objectives. Section 3 presents the proposed XAI methodology. Section 4 explains how the framework enables interpretable inference for both predictions and regression effects using deep neural networks. In Section 5, we assess the model’s performance through a series of simulation studies, followed by an application to the ABCD data in Section 6. Section 7 concludes with a discussion and future directions.

2 Imaging Data from Adolescent Brain Cognitive Development Study

This article explores a clinical application involving multimodal imaging data from children aged 9–10 years, collected as part of the Adolescent Brain Cognitive Development (ABCD) Study—the largest study of brain development in youth in the United States [Casey et al., 2018]. The primary aim is to investigate how local variability in resting-state fMRI (rs-fMRI) signals across time, reflecting the amplitude of low frequency oscillations, relates to a range of brain imaging predictors encompassing both structural brain characteristics and multi-task brain coactivation in response to several cognitive tasks. We begin by introducing our primary

scientific question and then describe the motivating ABCD imaging data.

2.1 Motivating Scientific Question

Functional magnetic resonance imaging (fMRI) captures blood-oxygen-level dependent (BOLD) signals in the brain while subjects are at rest or engaged in tasks, enabling the assessment of localized neuronal activity [Lv et al., 2018]. Fluctuations in the BOLD signal across time—typically quantified through variance or standard deviation of the time series—are now increasingly viewed as meaningful indicators of brain function rather than random noise, and are commonly interpreted as reflecting the amplitude of low-frequency fluctuations (ALFF) defined as the power of the BOLD signal between 0.01 and 0.10 Hz [Zuo et al., 2010, Hagler et al., 2019, Wang et al., 2021]. Existing studies have linked ALFF with structural properties of the brain (mean diffusivity and fractional anisotropy via diffusion MRI (dMRI) [Wang et al., 2021]; gray and white matter content assessed through structural MRI (sMRI) [Zuo et al., 2010]), patterns of functional connectivity within and between brain networks (rs-fMRI [Fu et al., 2017, Sheng et al., 2021, Di et al., 2013, Sato et al., 2019, Tomasi et al., 2016]), and response to task performance (task-based fMRI (t-fMRI) [Tomasi and Volkow, 2019]).

Building on this evidence, emerging findings in both computational and cognitive neuroscience suggest that ALFF serves as a marker of functional brain integrity, supports core processes of long distance information handling, and changes in response to task-activation [Zuo et al., 2010, Tomasi and Volkow, 2019]. The association of ALFF with both resting state networks and task-based brain activation is reinforced by the growing acceptance that resting state brain networks are associated with task-based activation and functional integration [Cole et al., 2016, Ye et al., 2022]. What is unclear from current work is how structural and network characteristics of the brain jointly contribute and explain variation in observed ALFF. Specifically, we are interested in modeling resting-state ALFF as a function of brain structure (cortical thickness and gray-white matter intensity contrasts measured via sMRI) and a multi-task coactivation network capturing coordinated patterns of brain activation during the execution of several cognitive tasks (measured via t-fMRI). In modeling variation in ALFF

from multiple images, it is highly desirable to provide interpretable mappings of each predictor modality onto the outcome as well as principled inference via uncertainty quantification in terms of model components and prediction.

With respect to statistical modeling, much of the current research on ALFF has concentrated on linking BOLD signal variability or ALFF distributions to either structural or functional brain characteristics by extracting targeted predictor variables from a *single* imaging modality and applying relatively straightforward statistical techniques. These investigations have included t-test comparisons of ALFF across regions dominated by gray versus white matter [Zuo et al., 2010], regional modeling of ALFF as a function of global white matter maturation through linear mixed effects models [Wang et al., 2021], linear regression modeling to associate ALFF with task-based activation maps [Tomasi and Volkow, 2019], and studies connecting ALFF to resting-state connectivity using statistical parametric mapping and correlational analyses of various functional graph metrics [Sheng et al., 2021, Di et al., 2013, Sato et al., 2019, Tomasi et al., 2016]. Recently, source localization has been used to associate low-frequency fluctuations captured by magnetoencephalography with ALFF derived from fMRI [Zhang et al., 2023b]. However, to the best of our knowledge, no study has yet attempted to jointly model ALFF using both structural and network images in order to evaluate their combined and independent association with ALFF despite growing evidence that each modality offers distinct yet complementary insights [Sui et al., 2012].

2.2 Clinical Imaging

We used data from the ABCD Study 5.0 Tabulated Release (<http://dx.doi.org/10.15154/8873-zj65>), focusing on baseline imaging measures from children aged 9–10 years. Imaging data were acquired and processed as outlined in [Hagler et al., 2019]. All images were aligned to the Montreal Neurological Institute (MNI) template space and parcellated to the Destrieux atlas (Figure 1(a); [Destrieux et al., 2010]) yielding 148 spatially defined regions of interests (ROIs) grouped into 12 nodes defined by brain hemisphere (left, right) and lobe (frontal, parietal, occipital, insula, and limbic). Thus, the data has hierarchical structure in which ROIs are organized

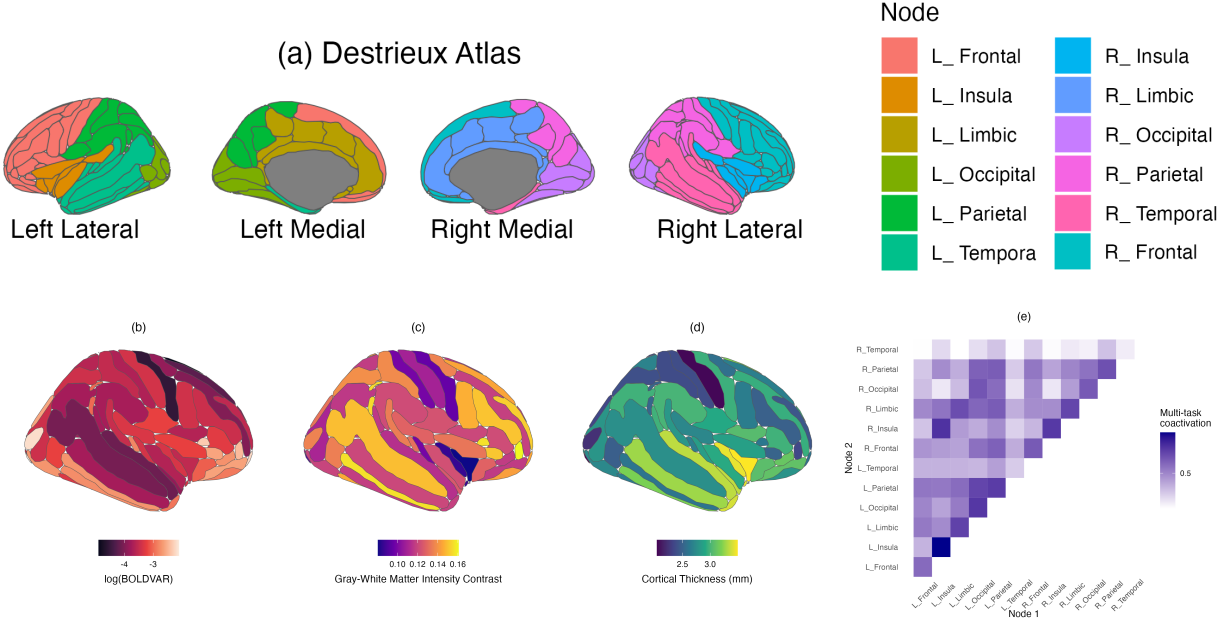


Figure 1: (a) The Destrieux atlas used to parcellate our motivating ABCD imaging data into 148 ROIs grouped by nodes defined by hemisphere (left, right) and lobes (frontal, parietal, occipital, insula, and limbic). (b) Outcome of interest: variance in the rs-fMRI BOLD time series (BOLDVAR) which is a proxy for amplitude of low frequency fluctuations (ALFF). (c) Structural predictor: cortical gray/white matter intensity contrast (GWMIC). (d) Structural predictor: cortical thickness (CT). (e) Network predictor: multi-task coactivation matrix representing brain coactivation across 12 nodes in response to an array of cognitive tasks.

within a collection of mutually exclusive nodes. Our outcome measure is the variance of the BOLD signal measured via rs-fMRI (BOLDVAR; Figure 1(b)) at each ROI which is considered a proxy for ALFF [Hagler et al., 2019] and is log transformed to better satisfy model assumptions discussed in Section 3. We consider two structural cortical predictors measured via sMRI at each ROI: cortical gray and white matter intensity contrasts (GWMIC; Figure 1(c)), thought to capture brain development, and cortical thickness (CT; Figure 1(d)), a local measure of gray matter thickness. We also consider a network image predictor which captures multi-task brain coactivation (Figure 1(e)), a measure of coordinated neuronal activation across entire brain while performing different tasks. Specifically, we obtained task-activation maps measuring local BOLD signals via t-fMRI (thought to reflect neuronal activity) collected on subjects while engaged in three tasks (money incentive delay task, stop signal task, and emotional version of the n-back task) with four contrasts per task yielding twelve task-activation maps as described

in [Ye et al., 2022, Casey et al., 2018, Hagler et al., 2019]. Based on the twelve task-activation maps, we constructed a correlation matrix among ROIs in the brain for each subject which we then averaged by node to yield a 12×12 multi-task coactivation matrix representing patterns of brain coactivation across hemispheres and lobes in response to a diverse array of tasks. To summarize, the outcome measure and two cortical structural predictors are observed at each ROI while the multi-task coactivation network predictor is observed for edges between brain nodes. Our primary aim is to expand the investigation of ALFF by integrating multimodal image-based predictors to better understand how structural and network-level factors together influence local variability in rs-fMRI signals. To address this, we introduce a multimodal regression framework to relate BOLDVAR to both structural and network images. The next section outlines this new regression strategy designed to accomplish these scientific aims.

3 Methodology

3.1 Notations

The dataset consists of n observations, each containing predictor and outcome images. For $i = 1, \dots, n$, let \mathbf{Z}_i denotes an undirected brain network, represented by a symmetric $V \times V$ matrix. Each entry $z_{i,(v,v')}$ quantifies the connectivity strength between functional nodes \mathcal{G}_v and $\mathcal{G}_{v'}$. These networks are undirected and contain no self-loops, so $z_{i,(v,v')} = z_{i,(v',v)}$, and $z_{i,(v,v)} = 0$. The V functional nodes are together denoted by $\mathcal{G} = \{\mathcal{G}_1, \dots, \mathcal{G}_V\}$. The v th node \mathcal{G}_v contains J_v ROIs, such that the total number of ROIs is $\sum_{v=1}^V J_v = J$. Let $y_i(\mathbf{s}_{v,j}) \in \mathbb{R}$ denote the spatial outcome, and $\mathbf{x}_i(\mathbf{s}_{v,j}) \in \mathbb{R}^Q$ represent the Q -dimensional spatial predictors at the j th ROI of the v th functional node for the i th individual. The spatial co-ordinate $\mathbf{s}_{v,j}$ of the j th ROI within the v th functional node is d -dimensional, where $d = 2, 3$, depending on whether the analysis covers the entire brain or a cross-section. The notation $\mathbf{a} \circ \mathbf{b}$ stands for the Hadamard product describing the elementwise product between two vectors \mathbf{a} and \mathbf{b} . In our context, $y_i(\mathbf{s}_{v,j})$ is the log-transformed BOLDVAR, $\mathbf{x}_i(\mathbf{s}_{v,j})$ represents the vector of GWMIC and CT, while \mathbf{Z}_i is the multi-task co-activation network matrix over brain functional nodes.

3.2 Proposed Explainable Artificially Intelligent (XAI) Model

We propose a two-stage modeling framework. In the first stage, we estimate the subject-specific overall network connectivity and nodal effects for each of the V functional nodes from brain networks of all subjects, capturing inter-nodal associations within a latent space. In the second stage, we introduce an explainable AI (XAI) framework that employs deep neural network architecture to generate predictive model for the outcome image, using spatial predictor images along with the estimated nodal effects.

3.3 First stage: Estimate Nodal Effects of the Network Predictor

The first stage of our framework fits a parsimonious probabilistic model to the edges of the undirected network predictor \mathbf{Z}_i , for subjects $i = 1, \dots, n$. Since the number of edges grows as $V(V - 1)/2$, the parameter space increases rapidly with the number of functional nodes. To address this, we represent node interactions within a lower-dimensional latent space that captures the network structure without imposing overly restrictive assumptions. Specifically, we model the edge probabilities as:

$$g^{-1}(E[z_{i,(v,v')}|\eta_i, \mathbf{u}_{i,v}, \mathbf{u}_{i,v'}, \sigma_i^2]) = \eta_i - \|\mathbf{u}_{i,v} - \mathbf{u}_{i,v'}\| + \epsilon_{i,(v,v')}, \quad \epsilon_{i,(v,v')} \sim N(0, \sigma_i^2), \quad (1)$$

where $g(\cdot)$ is a link function tailored to the type of edge weights (binary, categorical, or continuous). The parameter η_i captures overall degree of subject-specific network connectivity, while σ_i^2 denotes edge-level variability for the i th subject. The vector $\mathbf{u}_{i,v} = (u_{i,v,1}, \dots, u_{i,v,R})^T \in \mathbb{R}^R$ is a latent coordinate for functional node \mathcal{G}_v for the i th subject, encoding its position in an R -dimensional latent space. The strength of interaction between nodes \mathcal{G}_v and $\mathcal{G}_{v'}$ for subject i is modeled via the Euclidean distance between their latent positions $\mathbf{u}_{i,v}$ and $\mathbf{u}_{i,v'}$ —smaller distances indicate stronger interaction.

This latent space formulation reduces the number of parameters from $O(V^2)$ to $O(VR)$, where R is the intrinsic latent dimension. The value of R may be selected through cross-validation or more adaptive strategies [Guha and Rodriguez, 2021, Guhaniyogi and Dunson,

2016] at greater computational cost. As predictive performance is generally stable across a range of R , we opt for fixed R to maintain efficiency. Each subject’s network is modeled independently, fitting equation (1) separately for each i without pooling.

We assign a prior on each $\eta_i \sim N(0, 1)$ and the priors $\mathbf{u}_{i,v} \stackrel{i.i.d.}{\sim} N(\mathbf{0}, \mathbf{I}_R)$, $\sigma_i^2 \sim IG(\alpha, \beta)$, estimating the joint posterior distribution using Markov Chain Monte Carlo (MCMC) implemented in the `Nimble` software. Since the model (1) depends on the latent effects $\mathbf{u}_{i,v}$ ’s only through pairwise distances, it is invariant to the rotation of latent effects. We align estimates across MCMC samples to a common orientation by applying a “Procrustean transformation” [Borg and Groenen, 2005]. Posterior means of the aligned latent nodal estimate $\hat{\mathbf{u}}_{i,v}$ and posterior means of the estimate for the overall degree of network connectivity $\hat{\eta}_i$ are used as subject-level predictors in the second-stage regression model.

3.4 Second Stage: Additive Non-linear Regression Function Estimation through Deep Neural Network

In the second stage of our approach, we formulate a non-linear regression function to delineate association between the spatial outcome $y_i(\mathbf{s}_{v,j})$ and spatial predictors $\mathbf{x}_i(\mathbf{s}_{v,j})$, the estimated overall connectivity $\hat{\eta}_i$ and the estimated nodal effects $\hat{\mathbf{u}}_{i,v}$ corresponding to the v th functional node. Let the features from the network predictor be denoted by $\mathbf{g}_{i,v} = (\hat{\mathbf{u}}_{i,v}, \hat{\eta}_i)^T$. More precisely, our modeling approach involves

$$y_i(\mathbf{s}_{v,j}) = \beta_0 + \mathbf{x}_i(\mathbf{s}_{v,j})^T \boldsymbol{\beta}(\mathbf{s}_{v,j}) + h(\mathbf{g}_{i,v}) + \epsilon_i(\mathbf{s}_{v,j}), \quad j = 1, \dots, J_v; \quad v = 1, \dots, V, \quad (2)$$

where $\beta_0 \in \mathbb{R}$ is the intercept and the idiosyncratic errors are assumed to follow $\epsilon_i(\mathbf{s}_{v,j}) \stackrel{i.i.d.}{\sim} N(0, \tau^2)$. Here $h_v(\cdot)$ encodes the non-linear relationship between the outcome image at the j th ROI with spatial location $\mathbf{s}_{v,j}$ within the v th functional node, and $\hat{\mathbf{u}}_{i,v}$ and $\hat{\eta}_i$. The regression effects of spatial predictors $\mathbf{x}_i(\mathbf{s}_{v,j})$ is encoded in the coefficient vector $\boldsymbol{\beta}(\mathbf{s}_{v,j}) = (\beta_1(\mathbf{s}_{v,j}), \dots, \beta_Q(\mathbf{s}_{v,j}))^T \in \mathbb{R}^Q$ which also varies over spatial locations. They are referred to as varying-coefficient models (VCM), representing a flexible and popular extension of the linear

regression model [Hastie and Tibshirani, 1993]. VCMs combine the flexibility of non-parametric models to capture sufficiently complex dependencies between the outcome and predictors with the interpretability of parametric models, which makes them widely used in spatial data analysis [Gelfand et al., 2003, Guhaniyogi et al., 2022, 2024].

Traditionally, the functions $\beta(\cdot)$ and $h(\cdot)$ are modeled using Gaussian process (GP) priors; however, their estimation incurs high computational costs, scaling as $O(J^3)$ and $O(n^3)$ w.r.t. J and n , respectively. While basis function approximations offer computational efficiency [Morris, 2015, Reiss et al., 2017], they often result in over-smoothing. Recent advances in scalable GP methods have improved estimation for large datasets [Guhaniyogi et al., 2022, 2023], though they remain limited in providing fast, uncertainty-aware inference at the scale required for modern imaging studies with thousands of subjects and large number of brain regions.

There is a growing literature on standard deep neural networks (DNNs) to train dependency structures within spatial data [Li et al., 2023, Wikle and Zammit-Mangion, 2023], which not only reduces the computational complexity but also captures spatial dependency information. Therefore, for $q = 1, \dots, Q$, we can expand (2) to DNN as below:

$$\begin{aligned}\beta_q(\mathbf{s}_{v,j}) &= \sigma_{q,L_\beta}^{(\beta)} \left(\mathbf{W}_{q,L_\beta}^{(\beta)} \sigma_{q,L_\beta-1}^{(\beta)} \left(\dots \sigma_{q,2}^{(\beta)} \left(\mathbf{W}_{q,2}^{(\beta)} \sigma_{q,1}^{(\beta)} \left(\mathbf{W}_{q,1}^{(\beta)} \mathbf{s}_{v,j} + \mathbf{b}_{q,1}^{(\beta)} \right) + \mathbf{b}_{q,2}^{(\beta)} \right) \dots \right) + \mathbf{b}_{q,L_\beta}^{(\beta)} \right) \\ h(\mathbf{g}_{i,v}) &= \sigma_{L_h}^{(h)} \left(\mathbf{W}_{L_h}^{(h)} \sigma_{L_h-1}^{(h)} \left(\dots \sigma_2^{(h)} \left(\mathbf{W}_2^{(h)} \sigma_1^{(h)} \left(\mathbf{W}_1^{(h)} \mathbf{g}_{i,v} + \mathbf{b}_1^{(h)} \right) + \mathbf{b}_2^{(h)} \right) \dots \right) + \mathbf{b}_{L_h}^{(h)} \right)\end{aligned}\quad (3)$$

where $\sigma_{q,l_1}^{(\beta)}(\cdot)$ is an activation function of the l_1 th layer for the DNN construction of the coefficient function $\beta_q(\cdot)$, $l_1 = 1, \dots, L_\beta$, and $\sigma_{l_2}^{(h)}(\cdot)$ is an activation function of the l_2 th layer for the DNN representation of the function $h(\cdot)$, $l_2 = 1, \dots, L_h$. Assume that the l_1 th layer of the DNN construction of $\beta_q(\cdot)$ and l_2 th layer of DNN construction of $h(\cdot)$ include $k_{l_1}^{(\beta)}$ and $k_{l_2}^{(h)}$ neurons, respectively. The matrix $\mathbf{W}_{q,l_1}^{(\beta)} \in \mathbb{R}^{k_{l_1}^{(\beta)} \times k_{l_1-1}^{(\beta)}}$ is the weight parameters connecting the l_1 and $(l_1 - 1)$ th layer for the DNN constructions of $\beta_q(\cdot)$, and $\mathbf{W}_{l_2}^{(h)} \in \mathbb{R}^{k_{l_2}^{(h)} \times k_{l_2-1}^{(h)}}$ is the corresponding matrix connecting the l_2 and $(l_2 - 1)$ th layer for the DNN constructions $h(\cdot)$, respectively. The $k_{l_1}^{(\beta)}$ and $k_{l_2}^{(h)}$ dimensional vectors $\mathbf{b}_{q,l_1}^{(\beta)}$ and $\mathbf{b}_{l_2}^{(h)}$ are known as the bias parameters in the construction of DNN architectures for $\beta_q(\cdot)$ and $h(\cdot)$, respectively.

A traditional DNN approach proceeds by training the model by minimizing the following loss function with L_2 regularization terms as

$$\begin{aligned} \mathcal{L}_{\text{DNN}}(\boldsymbol{\theta}, \beta_0, \tau^2) = & \frac{1}{2N} \sum_{i=1}^n \sum_{v=1}^V \sum_{j=1}^{J_v} \frac{(y_i(\mathbf{s}_{v,j}) - \widehat{y}_i(\mathbf{s}_{v,j}))^2}{\tau^2} + \sum_{q=1}^Q \sum_{l_1=1}^{L_\beta} \lambda_{l_1}^{(W, \beta_q)} \left\| \mathbf{W}_{q, l_1}^{(\beta)} \right\|_2^2 \\ & + \sum_{q=1}^Q \sum_{l_1=1}^{L_\beta} \lambda_{l_1}^{(b, \beta_q)} \left\| \mathbf{b}_{q, l_1}^{(\beta)} \right\|_2^2 + \sum_{l_2=1}^{L_h} \lambda_{l_2}^{(W, h)} \left\| \mathbf{W}_{l_2}^{(h)} \right\|_2^2 + \sum_{l_2=1}^{L_h} \lambda_{l_2}^{(b, h)} \left\| \mathbf{b}_{l_2}^{(h)} \right\|_2^2, \quad (4) \end{aligned}$$

where $N = n \times J$, $J = \sum_{v=1}^V J_v$, and $\widehat{y}_i(\mathbf{s}_{v,j}) = \beta_0 + \mathbf{x}_i(\mathbf{s}_{v,j})^T \boldsymbol{\beta}(\mathbf{s}_{v,j}) + h(\mathbf{g}_{i,v})$ denote the point prediction from the model. Here $\boldsymbol{\theta} = \{(\mathbf{W}_{q, l_1}^{(\beta)}, \mathbf{b}_{q, l_1}^{(\beta)}) : q = 1, \dots, Q; l_1 = 1, \dots, L_\beta\} \cup \{(\mathbf{W}_{l_2}^{(h)}, \mathbf{b}_{l_2}^{(h)}) : l_2 = 1, \dots, L_h\}$ denotes the weights and bias parameters for the DNN architecture of $\beta_q(\cdot)$ and $h(\cdot)$. The parameters $\{(\lambda_{l_1}^{(W, \beta_q)}, \lambda_{l_1}^{(b, \beta_q)}) : l_1 = 1, \dots, L_\beta; q = 1, \dots, Q\}$ and $\{(\lambda_{l_2}^{(W, h)}, \lambda_{l_2}^{(b, h)}) : l_2 = 1, \dots, L_h\}$ are penalty parameters controlling shrinkage for weight and bias parameters. Equation 4 imposes regularization on the connections between layers, effectively minimizing the contribution of interconnections between many pair of neurons in two consecutive layers. This procedure prevents DNN from overfitting, and is popularly known as the *dropout architecture*. The aforementioned DNN framework offers a data-driven optimal point estimate $\widehat{\boldsymbol{\theta}}$ for the weight and bias parameters $\boldsymbol{\theta}$. However, it cannot quantify uncertainties, which are often central to statistical inference. To address this limitation, we leverage the connection between deep Gaussian processes and dropout-based deep neural networks, following Gal and Ghahramani [2016], to offer uncertainty quantification (UQ) in inference and prediction within the proposed framework.

3.4.1 Monte Carlo Dropout Architecture: Approximating a Deep Neural Network using Deep Gaussian Process

Notably, applying dropout before each layer in a deep neural network is equivalent to performing approximate inference in a deep GP marginalized over its covariance function. Specifically, the objective (4) minimizes the Kullback–Leibler divergence between an approximate distribution and the true posterior of a deep GP with a finite-rank covariance structure, as we show in our context in this section. This equivalence holds without simplifying assumptions, making the result broadly applicable to any neural network architecture that uses dropout.

Consider a sequence of random linear features $\{\psi_{(v,j)}^{(\beta,q,l_1)} \in \mathbb{R}^{k_{l_1}^{(\beta)}} : j = 1, \dots, J_v; v = 1, \dots, V; l_1 = 1, \dots, L_\beta\}$ over L_β layers, with the features in the l_1 th layer is of dimension $k_{l_1}^{(\beta)}$. Let $\Psi_{q,l_1}^{(\beta)} = \left[\psi_{(1,1)}^{(\beta,q,l_1)} : \dots : \psi_{(1,J_1)}^{(\beta,q,l_1)} : \dots : \psi_{(V,1)}^{(\beta,q,l_1)} : \dots : \psi_{(V,J_V)}^{(\beta,q,l_1)} \right]^T$ denotes a $J \times k_{l_1}^{(\beta)}$ dimensional matrix obtained by stacking features in the l_1 th layer. Let the k th column of this matrix is denoted as $\psi_{q,l_1,k}^{(\beta)}$. Assuming independence of $\Psi_{q,l_1}^{(\beta)}$ over k , we construct a deep GP with L_β layers as a generative model for $\beta_q(\cdot)$. Conditional on the previous layer, the finite-dimensional realizations at the l_1 th layer follow

$$\psi_{q,l_1,k}^{(\beta)} | \Psi_{q,l_1-1}^{(\beta)} \sim N(\mathbf{0}, \Sigma_{q,l_1}^{(\beta)}), \quad k = 1, \dots, k_{l_1}^{(\beta)}, \quad l_1 = 1, \dots, L_\beta, \quad (5)$$

with the coefficients $\beta_q(\mathbf{s}_{v,j})$ being constructed through the L_β th layer of the features. Specifically, if β_q is a J dimensional vector $(\beta_q(\mathbf{s}_{v,j}) : j = 1, \dots, J_v; v = 1, \dots, V)^T$, then we estimate $\beta_q = \sigma_{q,L_\beta}^{(\beta)}(\Psi_{q,L_\beta}^{(\beta)})$. The covariance matrix $\Sigma_{q,l_1}^{(\beta)} \in \mathbb{R}^{J \times J}$ for the finite dimensional realization depends on features from the previous layer, i.e., $\Sigma_{q,l_1}^{(\beta)} = \int \int \sigma_{q,l_1}^{(\beta)}(\Phi_{q,l_1-1}^{(\beta)} \mathbf{W}_{q,l_1}^{(\beta)\top} + \mathbf{b}_{q,l_1}^{(\beta)}) \sigma_{q,l_1}^{(\beta)}(\Phi_{q,l_1-1}^{(\beta)} \mathbf{W}_{q,l_1}^{(\beta)\top} + \mathbf{b}_{q,l_1}^{(\beta)})^\top p(\mathbf{W}_{q,l_1}^{(\beta)}) p(\mathbf{b}_{q,l_1}^{(\beta)}) d\mathbf{W}_{q,l_1}^{(\beta)} d\mathbf{b}_{q,l_1}^{(\beta)}$, where $\Phi_{q,l_1}^{(\beta)} = \left[\phi_{(1,1)}^{(\beta,q,l_1)} : \dots : \phi_{(1,J_1)}^{(\beta,q,l_1)} : \dots : \phi_{(V,1)}^{(\beta,q,l_1)} : \dots : \phi_{(V,J_V)}^{(\beta,q,l_1)} \right]^T$ is a $J \times k_{l_1}^{(\beta)}$ dimensional matrix of feature vectors after applying transformation through the activation function, such that $\phi_{(v,j)}^{(\beta,q,l_1)} = \sigma_{q,l_1}^{(\beta)}(\psi_{(v,j)}^{(\beta,q,l_1)})$. We approximate $\Sigma_{q,l_1}^{(\beta)}$ through Monte Carlo integration over a single realization, leading to

$$\widehat{\Sigma}_{q,l_1}^{(\beta)} = \sigma_{q,l_1}^{(\beta)}(\Phi_{q,l_1-1}^{(\beta)} \mathbf{W}_{q,l_1}^{(\beta)\top} + \mathbf{b}_{q,l_1}^{(\beta)}) \sigma_{q,l_1}^{(\beta)}(\Phi_{q,l_1-1}^{(\beta)} \mathbf{W}_{q,l_1}^{(\beta)\top} + \mathbf{b}_{q,l_1}^{(\beta)})^\top. \quad (6)$$

Similarly, define a sequence of random linear features $\{\psi_{(i,v)}^{(h,l_2)} \in \mathbb{R}^{k_{l_2}^{(h)}} : i = 1, \dots, n; v = 1, \dots, V; l_2 = 1, \dots, L_h\}$ and construct non-linear transformation $\{\phi_{(i,v)}^{(h,l_2)} : i = 1, \dots, n; v = 1, \dots, V; l_2 = 1, \dots, L_h\}$ of these features after applying the activation function, such that $\phi_{(i,v)}^{(h,l_2)} = \sigma_{l_2}^{(h)}(\psi_{(i,v)}^{(h,l_2)}) \in \mathbb{R}^{k_{l_2}^{(h)}}$. Collapsing the three-way tensor $\{\psi_{(i,v)}^{(h,l_2)}\}_{i=1,v=1}^{n,V} \in \mathbb{R}^{n \times V \times k_{l_2}^{(h)}}$ along the third mode leads to a $(nV) \times k_{l_2}^{(h)}$ matrix $\Psi_{l_2}^{(h)}$, where the k th column is denoted as $\psi_{l_2,k}^{(h)}$. Assuming independence of $\Psi_{l_2}^{(h)}$ across k , we construct a deep GP with L_h layers as a generative model for $h(\cdot)$. Conditional on the previous layer, the finite-dimensional realizations

of the l_2 th layer follows

$$\boldsymbol{\psi}_{l_2,k}^{(h)} | \boldsymbol{\Psi}_{l_2-1}^{(h)} \sim N(0, \boldsymbol{\Sigma}_{l_2}^{(h)}), \quad k = 1, \dots, k_{l_2}^{(h)}, \quad l_2 = 2, \dots, L_h, \quad (7)$$

with the non-linear function $h(\mathbf{g}_{i,v})$ being constructed through the L_h th layer of the features, i.e., if \mathbf{h} is a nV dimensional vector obtained by vectorizing the $n \times V$ dimensional matrix $(h(\mathbf{g}_{i,v}))_{i,v=1}^{n,V}$, then we estimate $\mathbf{h} = \sigma_{L_h}^{(h)}(\boldsymbol{\Psi}_{L_h}^{(h)})$. The form of the constructed covariance matrix $\boldsymbol{\Sigma}_{l_2}^{(h)} \in \mathbb{R}^{(nV) \times (nV)}$ is given by $\boldsymbol{\Sigma}_{l_2}^{(h)} = \int \int \sigma_{l_2}^{(h)}(\boldsymbol{\Phi}_{l_2-1}^{(h)} \mathbf{W}_{l_2}^{(h)\top} + \mathbf{b}_{l_2}^{(\beta)}) \sigma_{l_2}^{(h)}(\boldsymbol{\Phi}_{l_2-1}^{(h)} \mathbf{W}_{l_2}^{(h)\top} + \mathbf{b}_{l_2}^{(h)})^\top p(\mathbf{W}_{l_2}^{(h)}) p(\mathbf{b}_{l_2}^{(h)}) d\mathbf{W}_{l_2}^{(h)} d\mathbf{b}_{l_2}^{(h)}$, where $\boldsymbol{\Phi}_{l_2}^{(h)}$ is a $(nV) \times k_{l_2}^{(h)}$ matrix formed by collapsing the $n \times V \times k_{l_2}^{(h)}$ tensor $\{\boldsymbol{\phi}_{(i,v)}^{(h,l_2)}\}_{i,v=1}^{n,V}$ in the third mode. We approximate $\boldsymbol{\Sigma}_{l_2}^{(h)}$ through Monte Carlo integration over a single realization, leading to

$$\widehat{\boldsymbol{\Sigma}}_{l_2}^{(h)} = \sigma_{l_2}^{(h)}(\boldsymbol{\Phi}_{l_2-1}^{(h)} \mathbf{W}_{l_2}^{(h)\top} + \mathbf{b}_{l_2}^{(\beta)}) \sigma_{l_2}^{(h)}(\boldsymbol{\Phi}_{l_2-1}^{(h)} \mathbf{W}_{l_2}^{(h)\top} + \mathbf{b}_{l_2}^{(h)})^\top. \quad (8)$$

Assuming that the final layer in both generative models consists of one component, i.e., $k_{L_\beta}^{(\beta)} = k_{L_h}^{(h)} = 1$, we estimate the basis functions and basis coefficients using the features from the last layer, as described in the discussions succeeding equations (5) and (7), respectively. The proposed generative model is given by,

$$\begin{aligned} y_i(\mathbf{s}_{v,j}) | \{\boldsymbol{\Psi}_{q,L_\beta}^{(\beta)}\}_{q=1}^Q, \boldsymbol{\Psi}_{L_h}^{(h)}, \beta_0, \tau^2, \mathbf{x}(\mathbf{s}_i), \mathbf{g}_{i,v} &\sim N(\beta_0 + \mathbf{x}_i(\mathbf{s}_{v,j})^\top \boldsymbol{\beta}(\mathbf{s}_{v,j}) + h(\mathbf{g}_{i,v}), \tau^2), \\ \beta_q(\mathbf{s}_{v,j}) &= \sigma_{q,L_\beta}^{(\beta)}(\psi_{(v,j)}^{(\beta,q,L_\beta)}), \quad h(\mathbf{g}_{i,v}) = \sigma_{L_h}^{(h)}(\psi_{(i,v)}^{(h,L_h)}), \quad i = 1, \dots, n; \quad q = 1, \dots, Q; \quad j = 1, \dots, J_v; \quad v = 1, \dots, V \\ \boldsymbol{\psi}_{q,l_1,k}^{(\beta)} | \boldsymbol{\Psi}_{q,l_1-1}^{(\beta)} &\sim N(\mathbf{0}, \widehat{\boldsymbol{\Sigma}}_{q,l_1}^{(\beta)}), \quad q = 1, \dots, Q; \quad k = 1, \dots, k_{l_1}^{(\beta)}; \quad l_1 = 2, \dots, L_\beta \\ \boldsymbol{\psi}_{l_2,k}^{(h)} | \boldsymbol{\Psi}_{l_2-1}^{(h)} &\sim N(\mathbf{0}, \widehat{\boldsymbol{\Sigma}}_{l_2}^{(h)}), \quad k = 1, \dots, k_{l_2}^{(h)}, \quad l_2 = 2, \dots, L_h. \end{aligned} \quad (9)$$

Figure 2 illustrates the proposed explainable AI (XAI) approach.

Since it is not straightforward to make Bayesian inference for deep GP using MCMC, we adopt variational Bayesian inference called *MC dropout*, which is developed for deep GP based on MC approximation. Let $\mathbf{D} = \{\{\{\mathbf{x}_i(\mathbf{s}_{v,j}), \mathbf{s}_{v,j}, \mathbf{g}_{i,v}\}_{j=1}^{J_v}\}_{v=1}^V\}_{i=1}^n$ denote the input data. For

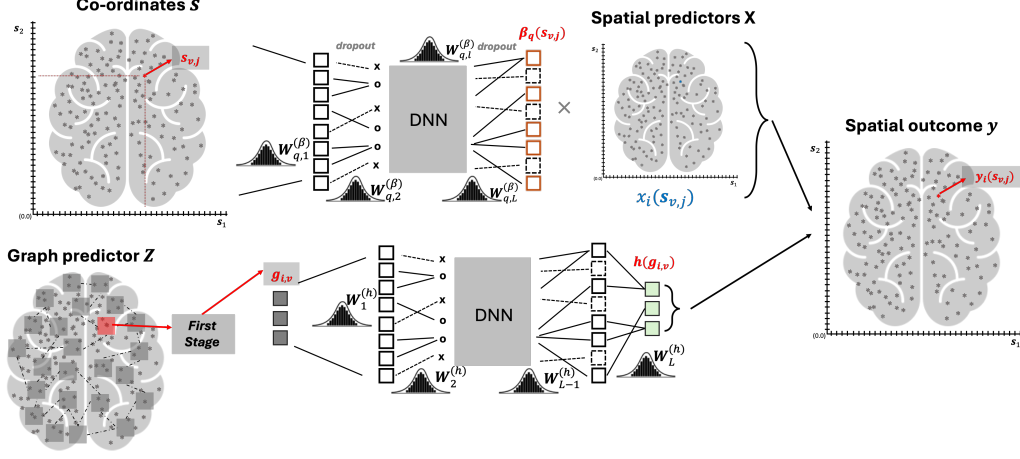


Figure 2: Illustration for the XAI.

Bayesian inference, independent normal priors are set on each component of the weight and bias parameters, denoted by $p(\mathbf{W}_{q,l_1}^{(\beta)})$, $p(\mathbf{b}_{q,l_1}^{(\beta)})$, $p(\mathbf{W}_{l_2}^{(h)})$, and $p(\mathbf{b}_{l_2}^{(h)})$. Denote the full prior distribution on the parameters θ by $p(\theta) = \prod_{l_1=1}^{L_\beta} \prod_{q=1}^Q p(\mathbf{W}_{q,l_1}^{(\beta)})p(\mathbf{b}_{q,l_1}^{(\beta)}) \prod_{l_2=1}^{L_h} p(\mathbf{W}_{l_2}^{(h)})p(\mathbf{b}_{l_2}^{(h)})$. We construct a variational approximation of the posterior distribution of parameters $\tilde{q}(\theta)$, constructed as $\tilde{q}(\theta) := \prod_{l_1=1}^{L_\beta} \prod_{q=1}^Q \tilde{q}(\mathbf{W}_{q,l_1}^{(\beta)})\tilde{q}(\mathbf{b}_{q,l_1}^{(\beta)}) \prod_{l_2=1}^{L_h} \tilde{q}(\mathbf{W}_{l_2}^{(h)})\tilde{q}(\mathbf{b}_{l_2}^{(h)})$, where

$$\begin{aligned} \tilde{q}(\mathbf{W}_{q,l_1}^{(\beta)}) &= \prod_{\forall t,p} \tilde{q}(w_{q,l_1,tp}^{(\beta)}), & \tilde{q}(\mathbf{b}_{q,l_1}^{(\beta)}) &= \prod_{\forall t} \tilde{q}(b_{q,l_1,t}^{(\beta)}), & \tilde{q}(\mathbf{W}_{l_2}^{(h)}) &= \prod_{\forall t,p} \tilde{q}(w_{l_2,tp}^{(h)}), & \tilde{q}(\mathbf{b}_{l_2}^{(h)}) &= \prod_{\forall t} \tilde{q}(b_{l_2,t}^{(h)}) \\ \tilde{q}(w_{q,l_1,tp}^{(\beta)}) &= p_{l_1}N(\mu_{q,l_1,tp}^{w,(\beta)}, \sigma^2) + (1 - p_{l_1})N(0, \sigma^2), & \tilde{q}(b_{q,l_1,t}^{(\beta)}) &= p_{l_1}N(\mu_{q,l_1,t}^{b,(\beta)}, \sigma^2) + (1 - p_{l_1})N(0, \sigma^2), \\ \tilde{q}(w_{l_2,tp}^{(h)}) &= p_{l_2}N(\mu_{l_2,tp}^{w,(h)}, \sigma^2) + (1 - p_{l_2})N(0, \sigma^2), & \tilde{q}(b_{l_2,t}^{(h)}) &= p_{l_2}N(\mu_{l_2,t}^{b,(h)}, \sigma^2) + (1 - p_{l_2})N(0, \sigma^2), \end{aligned} \quad (10)$$

where $l_1 = 1, \dots, L_\beta$ and $l_2 = 1, \dots, L_h$. The parameters $w_{q,l_1,tp}^{(\beta)}$ and $w_{l_2,tp}^{(h)}$ are the (t,p) th element of the weight matrices $\mathbf{W}_{q,l_1}^{(\beta)}$ and $\mathbf{W}_{l_2}^{(h)}$, respectively. Similarly, $b_{q,l_1,t}^{(\beta)}$ and $b_{l_2,t}^{(h)}$ are the t th element of the bias vectors $\mathbf{b}_{q,l_1}^{(\beta)}$ and $\mathbf{b}_{l_2}^{(h)}$, respectively. For the weight parameters, $\mu_{l_1,tp}^{w,(\beta)}$, $\mu_{l_2,tp}^{w,(h)}$ and σ^2 are variational parameters that control the mean and spread of the distributions, respectively. Let Δ denote the collection of variational parameters $\{\mu_{q,l_1,tp}^{w,(\beta)} : l_1 = 1, \dots, L_\beta; t = 1, \dots, k_{l_1}^{(\beta)}; p = 1, \dots, k_{l_1-1}^{(\beta)}; q = 1, \dots, Q\}$, $\{\mu_{l_2,tp}^{w,(h)} : l_2 = 1, \dots, L_h; t = 1, \dots, k_{l_2}^{(h)}; p = 1, \dots, k_{l_2-1}^{(h)}\}$, $\{\mu_{q,l_1,t}^{b,(\beta)} : l_1 = 1, \dots, L_\beta; t = 1, \dots, k_{l_1}^{(\beta)}; q = 1, \dots, Q\}$, $\{\mu_{l_2,t}^{b,(h)} : l_2 = 1, \dots, L_h; t = 1, \dots, k_{l_2}^{(h)}\}$ and

σ^2 . Under the mixture normal specification for the variational distribution of all weight and bias parameters, as the inclusion probability $p_l \in [0, 1]$ approaches 0, $\tilde{q}(w_{q,l_1,tp}^{(\beta)})$ and $\tilde{q}(w_{l_2,tp}^{(h)})$ becomes close to $N(0, \sigma^2)$, indicating a high likelihood of dropping the weight parameters (i.e., $w_{q,l_1,tp}^{(\beta)} = 0$ and $w_{l_2,tp}^{(h)} = 0$). We denote the variational distribution as $\tilde{q}(\boldsymbol{\theta}|\boldsymbol{\Delta})$ to explicitly show its dependence on the variational parameters. The optimal variational parameters are set by maximizing $\text{E}_{\tilde{q}}[\log(\pi(\boldsymbol{\theta}, \mathbf{D}))] - \text{E}_{\tilde{q}}[\log \tilde{q}(\boldsymbol{\theta}|\boldsymbol{\Delta})]$, the evidence lower bound (ELBO). The log ELBO of the deep GP is

$$\begin{aligned} \mathcal{L}_{\text{GP-VI}}(\beta_0, \tau^2, \boldsymbol{\Delta}) &= \sum_{i=1}^n \sum_{v=1}^V \sum_{j=1}^{J_v} \int \cdots \int \tilde{q}(\boldsymbol{\theta}|\boldsymbol{\Delta}) \log p(y_i(\mathbf{s}_{v,j})|\mathbf{x}_i(\mathbf{s}_{v,j}), \mathbf{g}_{i,v}, \beta_0, \tau^2, \{\boldsymbol{\Psi}_{q,L_\beta}^{(\beta)}\}_{q=1}^Q, \boldsymbol{\Psi}_{L_h}^{(h)}) \\ &\prod_{l_1=2}^{L_\beta} \prod_{q=1}^Q p(\boldsymbol{\Psi}_{q,l_1}^{(\beta)}|\boldsymbol{\Psi}_{q,l_1-1}^{(\beta)}, \mathbf{W}_{q,l_1}^{(\beta)}, \mathbf{b}_{q,l_1}^{(\beta)}) \prod_{l_2=2}^{L_h} p(\boldsymbol{\Psi}_{l_2}^{(h)}|\boldsymbol{\Psi}_{l_2-1}^{(h)}, \mathbf{W}_{l_2}^{(h)}, \mathbf{b}_{l_2}^{(h)}) d\mathbf{W}_{q,l_1}^{(\beta)} d\mathbf{b}_{q,l_1}^{(\beta)} d\mathbf{W}_{l_2}^{(h)} d\mathbf{b}_{l_2}^{(h)} \\ &- \text{KL}\left(\tilde{q}(\boldsymbol{\theta}|\boldsymbol{\Delta}) \parallel p(\boldsymbol{\theta})\right), \end{aligned} \quad (11)$$

where $p(\mathbf{y}_i(\mathbf{s}_{v,j})|\mathbf{x}_i(\mathbf{s}_{v,j}), \mathbf{g}_{i,v}, \beta_0, \tau^2, \boldsymbol{\Psi}_{q,L_\beta}^{(\beta)}, \boldsymbol{\Psi}_{L_h}^{(h)})$ is the data likelihood as obtained from equation (9). Note that $\boldsymbol{\Psi}_{q,L_\beta}^{(\beta)}$ and $\boldsymbol{\Psi}_{L_h}^{(h)}$ are dependent on the weight and bias parameters $\{\mathbf{W}_{q,l_1}^{(\beta)}, \mathbf{b}_{l_1}^{(\beta)}\}_{l_1=1}^{L_\beta}$ and $\{\mathbf{W}_{l_2}^{(h)}, \mathbf{b}_{l_2}^{(h)}\}_{l_2=1}^{L_h}$, respectively. Hence, we represent $p(y_i(\mathbf{s}_{v,j})|\mathbf{x}_i(\mathbf{s}_{v,j}), \mathbf{g}_{i,v}, \beta_0, \tau^2, \boldsymbol{\Psi}_{q,L_\beta}^{(\beta)}, \boldsymbol{\Psi}_{L_h}^{(h)})$ as $p(y_i(\mathbf{s}_{v,j})|\mathbf{x}_i(\mathbf{s}_{v,j}), \mathbf{g}_{i,v}, \beta_0, \tau^2, \boldsymbol{\theta})$. With the expressions of $p(\boldsymbol{\Psi}_{q,l_1}^{(\beta)}|\boldsymbol{\Psi}_{q,l_1-1}^{(\beta)}, \mathbf{W}_{q,l_1}^{(\beta)}, \mathbf{b}_{q,l_1}^{(\beta)})$ and $p(\boldsymbol{\Psi}_{l_2}^{(h)}|\boldsymbol{\Psi}_{l_2-1}^{(h)}, \mathbf{W}_{l_2}^{(h)}, \mathbf{b}_{l_2}^{(h)})$ being normal likelihoods obtained from (9), an MC approximation of the log ELBO can be obtained as

$$\begin{aligned} \mathcal{L}_{\text{GP-MC}}(\beta_0, \tau^2, \boldsymbol{\Delta}) &= \frac{1}{M} \sum_{m=1}^M \sum_{i=1}^n \sum_{v=1}^V \sum_{j=1}^{J_v} \log p(\mathbf{y}_i(\mathbf{s}_{v,j})|\mathbf{x}_i(\mathbf{s}_{v,j}), \mathbf{g}_{i,v}, \beta_0, \tau^2, \boldsymbol{\theta}^{(m)}) \\ &- \text{KL}\left(\tilde{q}(\boldsymbol{\theta}|\boldsymbol{\Delta}) \parallel p(\boldsymbol{\theta})\right), \end{aligned} \quad (12)$$

where $\boldsymbol{\theta}^{(m)} = \{\{\mathbf{W}_{q,l_1}^{(\beta)(m)}, \mathbf{b}_{q,l_1}^{(\beta)(m)}\}_{l_1=1,q=1}^{L_\beta,Q}, \{\mathbf{W}_{l_2}^{(h)(m)}, \mathbf{b}_{l_2}^{(h)(m)}\}_{l_2=1}^{L_h}\}$ are MC samples from the variational distribution in (10).

Under the conditions where the number of neurons $k_{l_1}^{(\beta)}$ and $k_{l_2}^{(h)}$ are large, and σ in (10) is small, $\text{KL}\left(\tilde{q}(\boldsymbol{\theta}|\boldsymbol{\Delta}) \parallel p(\boldsymbol{\theta})\right)$ can be approximated as $\text{KL}\left(\tilde{q}(\boldsymbol{\theta}|\boldsymbol{\Delta}) \parallel p(\boldsymbol{\theta})\right) \approx \sum_{l_1=1}^{L_\beta} \sum_{q=1}^Q \frac{p_{l_1}}{2} (\|\boldsymbol{\mu}_{q,l_1}^{w,(\beta)}\|_2^2) +$

$\sum_{l_1=1}^{L_\beta} \sum_{q=1}^Q \frac{p_{l_1}}{2} (\|\boldsymbol{\mu}_{q,l_1}^{b,(\beta)}\|_2^2) + \sum_{l_2=1}^{L_h} \frac{p_{l_2}}{2} (\|\boldsymbol{\mu}_{l_2}^{w,(h)}\|_2^2) + \sum_{l_2=1}^{L_h} \frac{p_{l_2}}{2} (\|\boldsymbol{\mu}_{l_2}^{b,(h)}\|_2^2)$, upto a constant involving $k_{l_1}^{(\beta)}, k_{l_2}^{(h)}$ ($l_1 = 1, \dots, L_\beta; l_2 = 1, \dots, L_h$) and σ^2 . Here $\boldsymbol{\mu}_{q,l_1}^{w,(\beta)} = (\mu_{q,l_1,kk'}^{w,(\beta)} : k, k' = 1, \dots, k_{l_1}^{(\beta)})^T$, $\boldsymbol{\mu}_{l_2}^{w,(h)} = (\mu_{l_2,kk'}^{w,(h)} : k, k' = 1, \dots, k_{l_2}^{(h)})^T$, $\boldsymbol{\mu}_{l_1}^{b,(\beta)} = (\mu_{l_1,k}^{b,(\beta)} : k = 1, \dots, k_{l_1}^{(\beta)})^T$ and $\boldsymbol{\mu}_{l_2}^{b,(h)} = (\mu_{l_2,k}^{b,(h)} : k = 1, \dots, k_{l_2}^{(h)})^T$. Plugging $\text{KL}(\tilde{q}(\boldsymbol{\theta}|\boldsymbol{\Delta}) \parallel p(\boldsymbol{\theta}))$ approximation to (12), we have

$$\begin{aligned} \mathcal{L}_{\text{GP-MC}}(\beta_0, \tau^2, \boldsymbol{\Delta}) &\approx \frac{1}{M} \sum_{m=1}^M \sum_{i=1}^n \sum_{v=1}^V \sum_{j=1}^{J_v} \log p(\mathbf{y}_i(\mathbf{s}_{v,j}) | \mathbf{x}_i(\mathbf{s}_{v,j}), \mathbf{g}_{i,v}, \beta_0, \tau^2, \boldsymbol{\theta}^{(m)}) \\ &- \sum_{l_1=1}^{L_\beta} \sum_{q=1}^Q \frac{p_{l_1}}{2} (\|\boldsymbol{\mu}_{q,l_1}^{w,(\beta)}\|_2^2) - \sum_{l_1=1}^{L_\beta} \sum_{q=1}^Q \frac{p_{l_1}}{2} (\|\boldsymbol{\mu}_{q,l_1}^{b,(\beta)}\|_2^2) - \sum_{l_2=1}^{L_h} \frac{p_{l_2}}{2} (\|\boldsymbol{\mu}_{l_2}^{w,(h)}\|_2^2) - \sum_{l_2=1}^{L_h} \frac{p_{l_2}}{2} (\|\boldsymbol{\mu}_{l_2}^{b,(h)}\|_2^2). \end{aligned} \quad (13)$$

By setting $\lambda_l^{(W,\beta_q)}, \lambda_l^{(b,\beta_q)}, \lambda_l^{(W,h)}$, and $\lambda_l^{(b,h)}$ as $\frac{p_l}{2N}$, the loss function (13) becomes close to (4). Details of the derivation is supplied in the supplementary material. This reveals that optimizing a frequentist neural network with dropout, as specified by the objective function (4), is mathematically equivalent to estimating the optimal variational parameters $\boldsymbol{\Delta}$ from (13). Consequently, the formulation in (3) can be interpreted as a deep GP expressed through a neural network architecture, where the parameters are estimated via variational distributions defined in (10). To train the model, we employ stochastic gradient descent (SGD) to update the weights and biases in each layer by minimizing the loss function in (4), yielding an optimized parameter set $\hat{\boldsymbol{\theta}}$. Owing to the equivalence between the objectives in (13) and (4), the optimized value $\hat{\boldsymbol{\theta}}$ corresponds directly to the optimized value $\hat{\boldsymbol{\Delta}}$ of the variational parameter. Given that the dropout variance σ^2 is small, randomly generating dropout on each entry of weight and bias parameters in $\hat{\boldsymbol{\theta}}$ effectively simulates draws from the variational posterior for weights and biases in (10). Hence, they can also be viewed as posterior samples of the deep neural network architecture with dropout applied on each layer. Repeating this procedure F times yields F approximate posterior samples from the deep neural network, which are further used for posterior inference of model parameters and posterior predictive inference. Details of the algorithm are presented in Algorithm 1.

Algorithm 1: Explainable AI Algorithm

- 1 **Step 1:** Initialize parameters $\boldsymbol{\theta}$ at $\boldsymbol{\theta}^{(0)}$ and β_0 at $\beta_0^{(0)}$;
 - 2 **Step 2:** Find the optimal point estimates $\boldsymbol{\theta}$, β_0 using SGD;
 - 3 **for** $iter = 1$ **to** n_{iter} **do**
 - 4 Update $\boldsymbol{\theta}$, β_0 using SGD to minimize loss function in Eq. (4);
 - 5 **Return:** Optimized estimates $\hat{\boldsymbol{\theta}} = \left\{ \begin{array}{l} \{\widehat{\mathbf{W}}_{q,l_1}^{(\beta)}, \widehat{\mathbf{b}}_{q,l_1}^{(\beta)}\}_{l_1=1, q=1}^{L_\beta, Q} \\ \{\widehat{\mathbf{W}}_{l_2}^{(h)}, \widehat{\mathbf{b}}_{l_2}^{(h)}\}_{l_2=1}^{L_h} \end{array} \right\}, \hat{\beta}_0$;
 - 6 **Step 3:** Draw samples of $\boldsymbol{\theta}$ and τ^2 using dropout;
 - 7 **for** $f = 1$ **to** F **do**
 - 8 Sample dropout masks;
 - 9 For $l_1 = 1, \dots, L_\beta$, $q = 1, \dots, Q$, sample each entry of the dropout mask
 $\mathbf{M}_{q,l_1,1}^{(\beta)(f)} \in \mathbb{R}^{k_{l_1}^{(\beta)} \times k_{l_1}^{(\beta)-1}}$ for weights from Bernoulli($1 - p_{l_1}$) and $\mathbf{M}_{q,l_1,2}^{(\beta)(f)} \in \mathbb{R}^{k_{l_1}^{(\beta)}}$ for bias vectors from Bernoulli($1 - p_{l_1}$).
 - 10 Similarly, for $l_2 = 1, \dots, L_h$, sample each entry of the dropout mask
 $\mathbf{M}_{l_2,1}^{(h)(f)} \in \mathbb{R}^{k_{l_2}^{(h)} \times k_{l_2}^{(h)-1}}$ for weights from Bernoulli($1 - p_{l_2}$) and $\mathbf{M}_{l_2,2}^{(h)(f)} \in \mathbb{R}^{k_{l_2}^{(h)}}$ for bias vectors from Bernoulli($1 - p_{l_2}$).
 - 11 Apply masks element-wise to $\hat{\boldsymbol{\theta}}$ to obtain sparse $\boldsymbol{\theta}^{(f)}$;
 - 12 Compute $\beta_q(\mathbf{s}_{v,j})^{(f)}$ and $h(\mathbf{g}_{i,v})^{(f)}$ using Eq. (3) from $\boldsymbol{\theta}^{(f)}$;
 - 13 Compute variance:

$$\tau^{2(f)} = \frac{1}{n \sum_v J_v} \sum_{i=1}^n \sum_{v=1}^V \sum_{j=1}^{J_v} \left(y_i(\mathbf{s}_{v,j}) - \hat{\beta}_0 - \mathbf{x}_i(\mathbf{s}_{v,j})^T \boldsymbol{\beta}^{(f)}(\mathbf{s}_{v,j}) - h^{(f)}(\mathbf{g}_{i,v}) \right)^2$$
;
 - 14 **Step 4: return** *Approximate posterior samples:* $\{\boldsymbol{\theta}^{(1)}, \dots, \boldsymbol{\theta}^{(F)}\}, \{\tau^{2(1)}, \dots, \tau^{2(F)}\}$;
-

4 Explainable Inference with Deep Neural Network

A key feature of XAI is its ability to quantify uncertainty in the estimation of the spatially-varying image predictor coefficients $\beta_q(\cdot)$, the function representing node effects $h(\cdot)$, and in the prediction of the outcome image, thereby enabling *explainable inference* within deep neural networks. Let $\mathbf{D} = \{(y_i(\mathbf{s}_{v,j}), \mathbf{x}_i(\mathbf{s}_{v,j}), \mathbf{g}_{i,v})^T : i = 1, \dots, n; j = 1, \dots, J_v; v = 1, \dots, V\}$ denote the observed data. To predict unobserved outcome $y_{i^*}(\mathbf{s}_{v,j})$ for a new sample indexed i^* , we first employ the algorithm outlined in Section 3.3 to construct the features $\{\mathbf{g}_{i^*,v} : v = 1, \dots, V\}$ from the graph predictor \mathbf{Z}_{i^*} for the new sample. The posterior predictive distribution is then given by $p(y_{i^*}(\mathbf{s}_{v,j}) | \mathbf{D}) = \int \cdots \int N(y_{i^*}(\mathbf{s}_{v,j}) | \beta_0 + \mathbf{x}_{i^*}(\mathbf{s}_{v,j})^T \boldsymbol{\beta}(\mathbf{s}_{v,j}) + h(\mathbf{g}_{i^*,v}), \tau^2) \pi(\boldsymbol{\theta} | \mathbf{D}) d\boldsymbol{\theta} d\beta_0 d\tau^2$. Since it is challenging to compute the posterior predictive distribution directly, we approximate it through the samples of $\boldsymbol{\theta}, \beta_0, \tau^2$. With approximate posterior samples $\{\boldsymbol{\theta}^{(f)}, \beta_0^{(f)}, \tau^{2(f)}\}_{f=1}^F$

drawn following Algorithm 1, we adopt composition sampling, wherein the f th post burn-in iterate $y_{i^*}^{(f)}(\mathbf{s}_{v,j})$ is drawn from $N(y_{i^*}(\mathbf{s}_{v,j})|\beta_0^{(f)} + \mathbf{x}_{i^*}(\mathbf{s}_{v,j})^T \boldsymbol{\beta}(\mathbf{s}_{v,j})^{(f)} + h(\mathbf{g}_{i^*,v})^{(f)}, \tau^{2(f)})$.

Inference on $h(\mathbf{g}_{i,v})$ can be obtained from the approximate posterior samples of $\{h(\mathbf{g}_{i,v})^{(f)}\}_{f=1}^F$ which are obtained from (3) using samples $\{\boldsymbol{\theta}^{(f)}\}_{f=1}^F$. Although inference on $\beta_q(\mathbf{s}_{v,j})$ can be performed directly from its approximate posterior samples $\{\beta_q(\mathbf{s}_{v,j})^{(f)} : f = 1, \dots, F\}$, our empirical analysis indicates slight under-coverage in the resulting credible intervals. To mitigate this, we propose approximating the posterior distribution of $\beta_q(\mathbf{s}_{v,j})$ with a normal distribution. The mean and variance of this normal distribution are given by, $\mu_q(\mathbf{s}_{v,j}) = \frac{1}{F} \sum_{f=1}^F \beta_q(\mathbf{s}_{v,j})^{(f)}$ and $\sigma_q^2(\mathbf{s}_{v,j}) = \frac{1}{F-1} \sum_{f=1}^F (\beta_q(\mathbf{s}_{v,j})^{(f)} - \mu_q(\mathbf{s}_{v,j}))^2$, respectively. We then generate refined approximate posterior samples of $\beta_q(\mathbf{s}_{v,j})$ by drawing from the normal distribution $N(\mu_q(\mathbf{s}_{v,j}), \sigma_q^2(\mathbf{s}_{v,j}))$.

5 Simulation Study

This section evaluates the performance of XAI alongside relevant Bayesian linear, non-linear, and deep learning methods for image-on-image regression, focusing on three key aspects: predictive inference, inference on the spatially-varying predictor coefficients $\boldsymbol{\beta}_q(\cdot)$, and inference on $h(\cdot)$, which captures the non-linear effect of the network predictor.

5.1 Simulation Design

In all simulations, the spatial locations $\mathbf{s}_{v,j}$ are assumed to be three-dimensional ($d = 3$) and are drawn uniformly from the domain $[0, 2] \times [0, 2] \times [0, 2]$, for $v = 1, \dots, V$ and $j = 1, \dots, J_v$. Each simulation assumes $Q = 2$, sets $\mathbf{x}_i(\mathbf{s}_{v,j}) = \mathbf{x}_i \in \mathbb{R}^Q$ for all v, j , and draws \mathbf{x}_i from $N(0, \mathbf{I}_2)$.

The spatial predictor coefficients in $\beta_q(\cdot)$ ($q = 1, 2$) are simulated from a Gaussian process (GP) with mean zero and an exponential covariance function, characterized by the spatial variance $\delta_{\beta,q}^2$ and the spatial scale parameter $\eta_{\beta,q}$. Specifically, $\text{Cov}(\beta_q(\mathbf{s}_{v,j}), \beta_q(\mathbf{s}_{v',j'})) = \delta_{\beta,q}^2 \exp(-\|\mathbf{s}_{v,j} - \mathbf{s}_{v',j'}\|_2 / \eta_{\beta,q})$, for any $v, v' = 1, \dots, V$, $j = 1, \dots, J_v$ and $j' = 1, \dots, J_{v'}$. The latent network effects $\mathbf{g}_{i,v}$'s are simulated from $N(0, \mathbf{I}_2)$. The regression function $h(\cdot)$ for the network predictor is modeled as a Gaussian process (GP) with mean zero and an exponential covariance kernel, defined by the spatial variance parameter δ_h^2 and spatial scale parameter η_h ,

$\text{Cov}(h(\mathbf{g}_{i,v}), h(\mathbf{g}_{i',v'})) = \delta_h^2 \exp(-\|\mathbf{g}_{i,v} - \mathbf{g}_{i',v'}\|_2/\eta_h)$, $i, i' = 1, \dots, n$ and $v, v' = 1, \dots, V$. Each simulation uses a sample size of 300 with low signal-to-noise ratio (SNR) to reflect real neuroimaging data. The response is generated using equation (2) with noise variance $\tau^2 = 4$. Of the 300 samples, 180 are used for training, 60 for validation, and $n^* = 60$ for testing. The model is built using both training and validation sets. Simulations assume equal regions per node, i.e., $J_1 = \dots = J_V$, and fix the number of network nodes at $V = 30$.

We explore multiple simulation scenarios, by varying key factors such as the degree of spatial correlation among predictor coefficients and the number of regions per node. Additionally, different combinations of $(\delta_{\beta,1}^2, \delta_{\beta,2}^2, \eta_{\beta,1}, \eta_{\beta,2}, \delta_h^2, \eta_h)$ result in significantly different variability, which allows us to evaluate model performance under a range of SNR conditions, testing its robustness across different cases.

5.2 Competitors and Metric of Comparison

We implement our XAI approach using TensorFlow, an open-source machine learning platform. All experiments were conducted on a 4-core, 2.3 GHz Intel Core i7 processor. The detailed configuration of the deep neural network, including the loss function, activation function, and tuning parameters, is provided in the supplementary materials.

To evaluate XAI, we compare its predictive inference, estimation of regression coefficients $\beta_q(\cdot)$ and network effect $h(\cdot)$ against several competing methods: Bayesian Additive Regression Trees (BART) [Chipman et al., 2010], Bayesian Image-on-Image Regression via Deep Kernel Learning-based Gaussian Processes (BIRD-GP) [Ma et al., 2023], and Generalized Linear Model (GLM). While fitting the BART, along with the imaging predictor and network latent effects, we add spatial co-ordinates as covariates for a fair comparison. GLM is a common method for image-on-image regression [Batouli and Sisakhti, 2020] but fails to incorporate structural information or model non-linear relationships, and does not offer uncertainty. BART stacks the spatial and vectorized network predictors together as a single input, without accounting for their structural differences. BIRD-GP projects input and response images into a lower-dimensional space using GP, with bases trained via a deep neural network to enhance interpretability. It then

applies non-linear regression between the projected images for prediction and uncertainty quantification. However, unlike XAI, BIRD-GP vectorizes the network predictor without leveraging its inherent structure, which may limit its ability to capture complex dependencies. BART is fitted using R packages BART[Sparapani et al., 2021] and BIRD-GP is fitted using Python codes from authors.

To assess predictive performance, we report root mean square prediction error (RMSPE), empirical coverage, and average length of 95% prediction intervals over n^* out-of-sample observations. For estimation accuracy, root mean square error (RMSE), coverage, and interval length are reported for each $\beta_q(\cdot)$ and $h(\cdot)$, with point estimates taken as posterior means for Bayesian models and as point estimates for frequentist models. Inference on $\beta_q(\cdot)$ and $h(\cdot)$ is only available for XAI and GLM, as BART and BIRD-GP are not designed to provide such inference. Each simulation case is replicated 100 times.

5.3 Simulation Results

5.3.1 Impact of Changing the Total Number of ROIs (J)

To evaluate the impact of cell-level sample size, we consider four simulation cases by varying the total number of ROIs J between 150 to 1200 across four cases (see Table 1). For all four cases, the variance parameters and scale parameters are kept fixed at $(\delta_{\beta,1}^2, \delta_{\beta,2}^2, \delta_h^2) = (2, 1, 2.5)$ and $(\eta_{\beta,1}, \eta_{\beta,2}, \eta_h) = (5, 4, 6)$.

Figure 3 shows that XAI consistently yields lower RMSE than GLM across varying values of J when estimating $\beta_1(\mathbf{s})$, $\beta_2(\mathbf{s})$ and $h(\mathbf{g})$. While GLM assumes a linear relationship between the network latent effect and the outcome, XAI flexibly captures complex nonlinear dependencies through its estimation of the nonlinear function $h(\mathbf{g})$. Furthermore, the GLM framework fits separate regression coefficients for each ROI without leveraging spatial correlations, resulting in stable but less adaptive point estimates with decreasing standard errors as J increases. In contrast, XAI exhibits notable improvements in estimation accuracy with larger J , owing to its ability to borrow information spatially for estimating $\beta_1(\mathbf{s})$ and $\beta_2(\mathbf{s})$, and across the network latent space for $h(\mathbf{g})$.

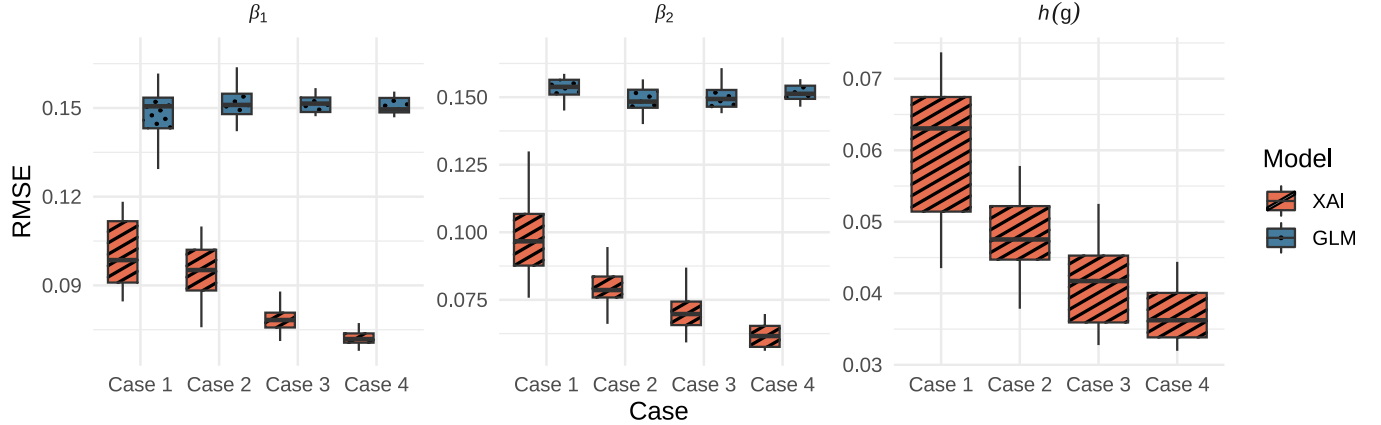


Figure 3: Root mean squared error (RMSE) comparison between the proposed XAI method and GLM for estimating the spatially varying coefficients $\beta_1(\mathbf{s})$ and $\beta_2(\mathbf{s})$, and the network latent effect $h(\mathbf{g})$ under Case 1 to Case 4. Boxplots show the distribution of RMSE across 100 simulation replications. The inference on $\beta_1(\mathbf{s})$, $\beta_2(\mathbf{s})$, $h(\mathbf{g})$ are not available for BART and BIRD-GP. The inference on $h(\mathbf{g})$ is not available for GLM.

Table 1: Prediction performance comparison for simulated datasets under Case 1 to Case 4. The table reports the root mean squared prediction error (RMSPE) with standard errors in parentheses for each method (XAI, BART, BIRD-GP, and GLM). The standard errors are presented over 100 replications. Best performing model is boldfaced in each case.

J	Cases	XAI	BART	BIRD-GP	GLM
150	Case 1	2.0101(0.011)	2.0148(0.010)	3.0234(1.0993)	2.0264(0.011)
300	Case 2	2.0020(0.011)	2.0093(0.010)	2.6435(0.4559)	2.0247(0.007)
600	Case 3	2.0024(0.008)	2.0086(0.005)	2.6155(0.4028)	2.0267(0.005)
1200	Case 4	2.0038(0.007)	2.0065(0.004)	2.7359(0.6534)	2.0246(0.004)

Table 1 presents the root mean squared prediction error (RMSPE) for the competing models, averaged over 100 replications, with standard errors provided in parentheses. Across varying values of J , the point prediction performance of XAI, BART, and GLM remains stable. XAI achieves comparable accuracy to BART and GLM, while significantly outperforming the deep learning alternative BIRD-GP. As shown in Figure 4, both XAI and BIRD-GP attain near-nominal coverage; however, XAI produces noticeably narrower predictive intervals. A closer inspection reveals that all four simulation scenarios assume a signal-to-noise ratio (SNR) below 1—reflective of the conditions in the real data application (Section 6)—with a sample size of $n = 300$. Due to its greater data requirements, BIRD-GP performs substantially worse than XAI under these settings, although the performance gap narrows as n and SNR increase. Meanwhile,

BART severely underestimates uncertainty, yielding the narrowest predictive intervals and the lowest coverage among all competing methods.

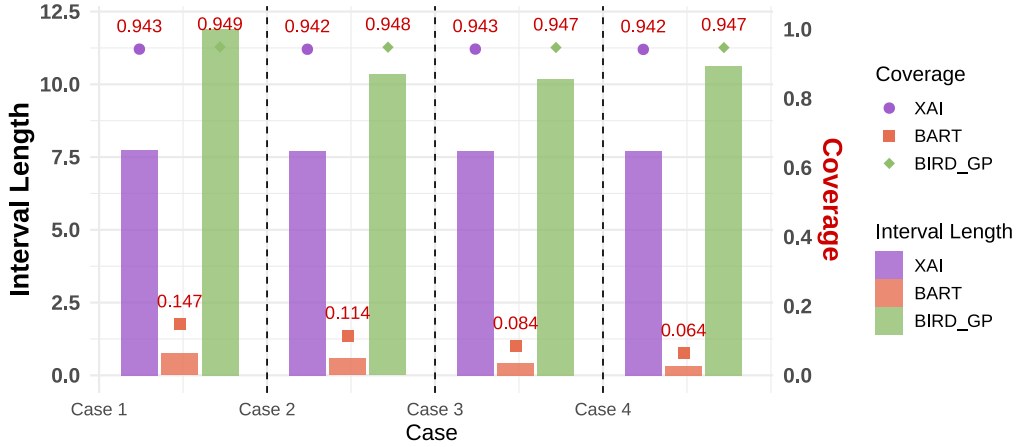


Figure 4: Coverage and length of 95% predictive intervals averaged over replications for XAI, BIRD-GP and BART. They are not available for GLM. Results show near nominal coverage of XAI with smaller predictive intervals than BIRD-GP.

5.3.2 Impact of Changing Signal-to-noise Ratios (SNRs)

To investigate the effect of different signal-to-noise ratios (SNRs), we design simulation scenarios by varying the variance parameters $\delta_{\beta,1}^2$, $\delta_{\beta,2}^2$ and δ_h^2 corresponding to the regression functions $\beta_1(\cdot)$, $\beta_2(\cdot)$, and $h(\cdot)$ while fixing the total number of ROIs at $J = 600$ and the number of nodes at $V = 30$. As shown in Table 2, increasing SNR corresponds to stronger spatial signals relative to noise.

Table 2: Prediction performance comparison for simulated datasets under Case 5 to Case 7 for varying signal-to-noise ratio (SNR), by varying the variance parameters $\delta_{\beta,1}^2$, $\delta_{\beta,2}^2$, δ_h^2 , while fixing the number of nodes (V) and the total number of ROIs (J). The table reports the root mean squared prediction error (RMSPE) with standard errors in parentheses for each method (XAI, BART, BIRD-GP and GLM). The standard errors are presented over 100 replications. Best performing model is boldfaced in each case.

$\delta_{\beta,1}^2$	$\delta_{\beta,2}^2$	δ_h^2	SNR	Cases	XAI	BART	BIRD-GP	GLM
2	1	1	0.42	Case 5	2.0020(0.009)	2.0080(0.005)	2.5549(0.382)	2.0267(0.005)
4	3	3	0.69	Case 6	2.0037(0.008)	2.0120(0.005)	2.9983(0.646)	2.0312(0.006)
5	6	5	0.81	Case 7	2.0052(0.008)	2.0155(0.005)	3.3656(0.782)	2.0358(0.008)

Figure 5 highlights the superior performance of XAI over GLM in estimating the varying coefficients $\beta_1(\mathbf{s})$, $\beta_2(\mathbf{s})$ and the non-linear function encoding network latent effect $h(\mathbf{g})$. With

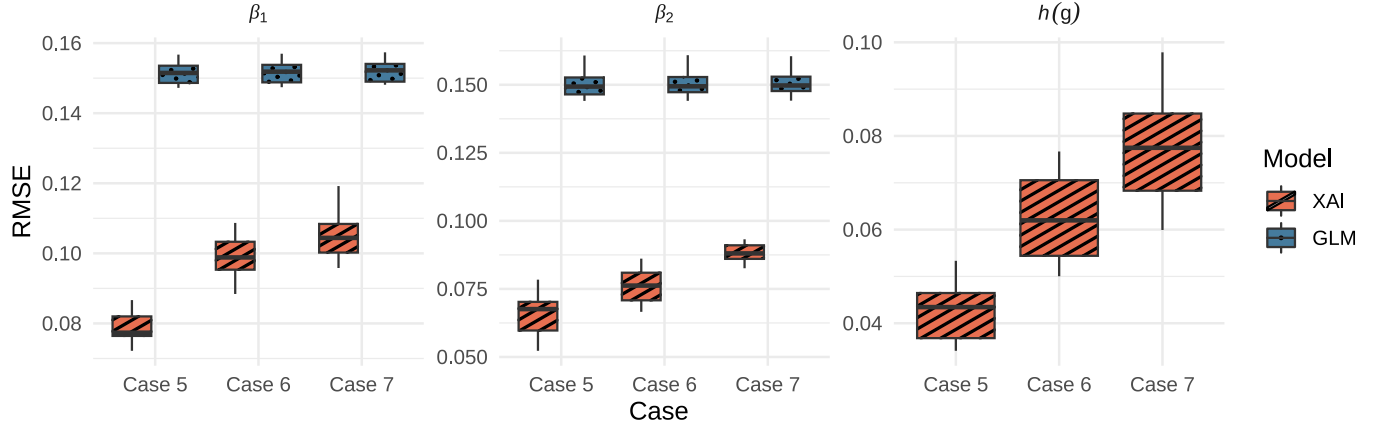


Figure 5: Root mean squared error (RMSE) comparison between the proposed XAI method and GLM for estimating the spatially varying coefficients $\beta_1(\mathbf{s})$ and $\beta_2(\mathbf{s})$, and the network latent effect $h(\mathbf{g})$ under Case 1 to Case 4. Boxplots show the distribution of RMSE across 100 simulation replications. The inference on $\beta_1(\mathbf{s})$, $\beta_2(\mathbf{s})$, $h(\mathbf{g})$ are not available for BART and BIRD-GP. The inference on $h(\mathbf{g})$ is not available for GLM.

changing SNR, GLM’s performance remains relatively unchanged, and the performance gap between GLM and XAI tends to get smaller with increasing SNR from Case 5 to 7. Since Cases 5–7 correspond to overall low SNR settings, XAI substantially outperforms its deep learning competitor BIRD-GP in terms of point prediction, as reflected in Table 2. Additionally, both BIRD-GP and XAI achieve near-nominal predictive coverage, although BIRD-GP produces credible intervals nearly twice as wide as those of XAI, as shown in Figure 6. BART provides comparable point prediction but severely underestimates predictive uncertainty, leading to overly narrow credible intervals.

5.3.3 Impact of Changing Correlation Parameters

To assess the impact of varying spatial correlation, we vary the spatial scale parameters $\eta_{\beta,1}$, $\eta_{\beta,2}$, and η_h (see Table 3) while keeping the variance parameters fixed. Increasing the scale parameters induces stronger association, allowing us to evaluate how model performance changes with the degree of association in $\beta_1(\cdot)$, $\beta_2(\cdot)$, and $h(\cdot)$.

An increase in the long-range dependence from Case 8-10 becomes less favorable to GLM that does not incorporate dependence, leading to an increasing performance gap between GLM and XAI in terms of estimating spatially varying coefficients $\beta_1(\mathbf{s})$, $\beta_2(\mathbf{s})$ and the function $h(\mathbf{g})$,

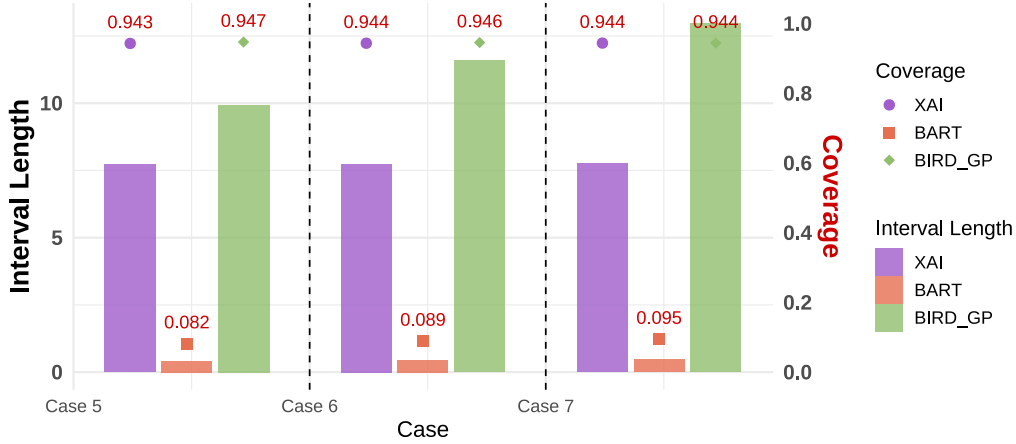


Figure 6: Coverage and length of 95% predictive intervals averaged over replications for XAI, BIRD-GP and BART. They are not available for GLM. Results show near nominal coverage of XAI with smaller predictive intervals than BIRD-GP.

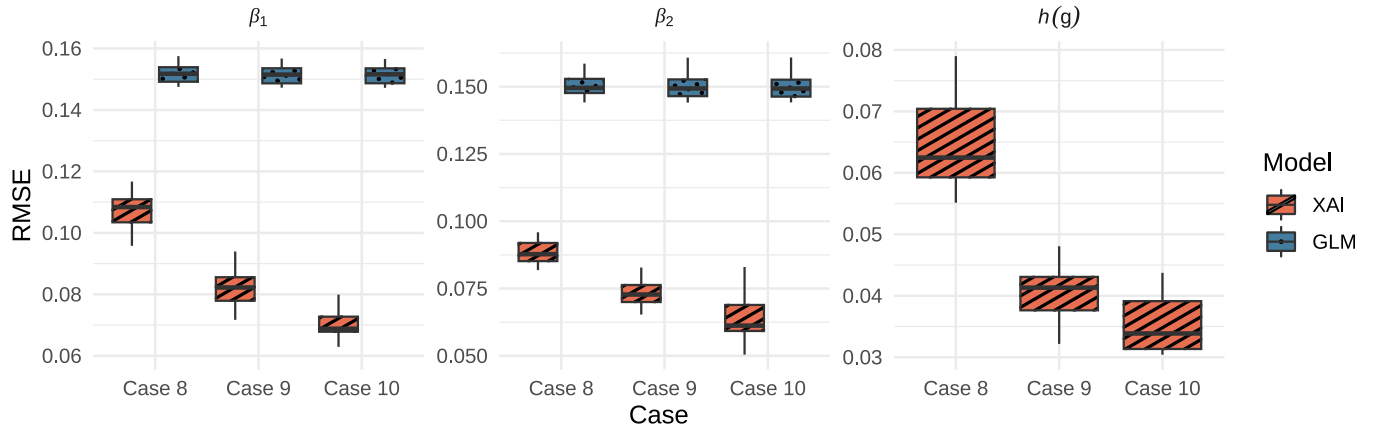


Figure 7: Root mean squared error (RMSE) comparison between the proposed XAI method and GLM for estimating the spatially varying coefficients $\beta_1(\mathbf{s})$ and $\beta_2(\mathbf{s})$, and the function encoding network latent effect $h(\mathbf{g})$ under Case 8 to Case 10. Boxplots show the distribution of RMSE across 100 simulation replications. The inference on $\beta_1(\mathbf{s})$, $\beta_2(\mathbf{s})$, $h(\mathbf{g})$ are not available for BART and BIRD-GP. The inference on $h(\mathbf{g})$ is not available for GLM.

as evident in Figure 7. As shown in Table 3 and Figure 8, XAI outperforms BIRD-GP in point prediction, and allows narrower predictive intervals with a similar coverage. As before, BART performs comparably in terms of point prediction but underestimates uncertainty.

Computation Time. In the XAI model, computation time is mainly driven by the sample size (n) and the total number of ROIs across all functional nodes (J). To examine how computational complexity scales with n and J , we fit the model for combinations of

Table 3: Prediction performance comparison for simulated datasets under Case 8 to Case 10, by varying the scale parameters $\eta_{\beta,1}, \eta_{\beta,2}, \eta_h$, while fixing the variance parameters. The table reports the root mean squared prediction error (RMSPE) with standard errors in parentheses, for each method (XAI, BART, BIRD-GP, and GLM). The standard errors are computed over 100 replications.

$\eta_{\beta,1}$	$\eta_{\beta,2}$	η_h	Cases	XAI	BART	BIRD-GP	GLM
2	3	3	Case 8	2.0048(0.005)	2.0150(0.005)	2.6311(0.391)	2.0339(0.007)
5	6	5	Case 9	2.0025(0.006)	2.0086(0.005)	2.6171(0.400)	2.0267(0.005)
7	8	8	Case 10	2.0017(0.006)	2.0072(0.005)	2.6136(0.409)	2.0259(0.004)

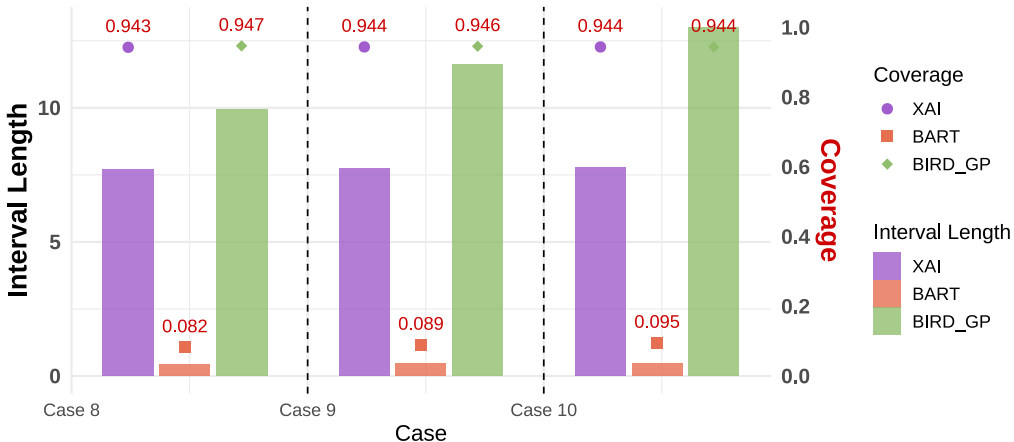


Figure 8: Coverage and length of 95% predictive intervals averaged over replications for XAI, BIRD-GP and BART. They are not available for GLM. Results show near nominal coverage of XAI with smaller predictive intervals than BIRD-GP.

$J = 100, 300, 500, 1000$ and $n = 300, 1000, 3000, 5000$. Each model was trained for 200 epochs with a batch size of 64, and uncertainty was quantified using MC dropout with $F = 200$ samples. As shown in Figure 9, computation time grows linearly with both n and J . For instance, full inference with $n = 5000$ and $J = 300$ completes in under 5 minutes.

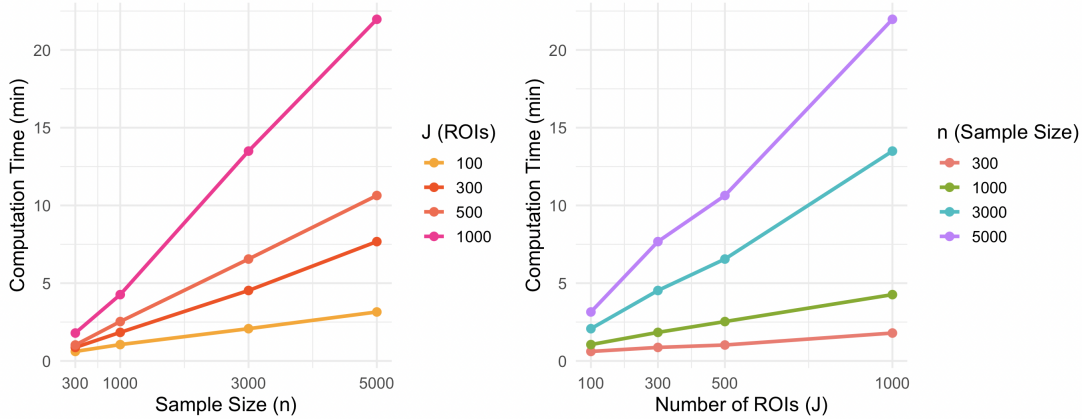


Figure 9: Computation time (in minutes) for XAI under varying dimensions of input data. Left: Computation time as a function of sample size n for different numbers of ROIs J . Right: Computation time as a function of the number of ROIs J for different sample size n .

6 Application to the Multi-modal ABCD Data

6.1 Data Structure and Methods

We apply our proposed method to the ABCD dataset to answer our motivating scientific question described in Section 2. Each participant is observed with two structural images containing 148 ROIs and these ROIs are mapped to a 3-dimensional space using 3-dimensional coordinates obtained from the R package `brainGraph` [Watson, 2020]. To facilitate interpretation of the targeted varying coefficient functions across ROIs, we scale the outcome and local covariates within each ROI to have standard deviation (SD) of one across subjects. This linear scaling yields standardized regression coefficients that are directly comparable across ROIs allowing us to compare effects in terms of SD units. To incorporate the network structure into our model, we employ a latent space model described in Section 3.3, which generates 3-dimensional latent variables representing the network. For the network nodes, we define each node as a sub-group of ROIs organized based on similar connectivity patterns. This hierarchical approach efficiently reduces the overall network complexity, allowing us to model the structure using only 12 nodes, despite the initial set containing 148 ROIs. Additionally, the degree of connectivity for each network image, estimated as the intercept of the latent space model, is

integrated into the framework.

Our analysis uses a total of $N = 4,850$ participants for model fitting, $N_{\text{val}} = 1,618$ participants for validation, and $N_{\text{test}} = 1,618$ participants for testing. Note that we utilized validation data to find out the optimized tuning hyper-parameters such as batch size, learning rate, and number of layers. Similar to simulation studies, we compare our inferential performance, as well as the total computation time (includes time for training, validation and prediction), for the proposed approach with BIRD-GP, BART and GLM.

6.2 Data Analysis Results

We present the results from our application of the proposed XAI model to the multi-modal ABCD imaging data. Figure 10 displays lateral and medial cross sections of the posterior (a) mean and (b) 95% credible interval length for the spatially varying coefficient function $\beta_1(\mathbf{s}_{v,j})$ capturing effects of GWMIC. Positive (negative) regression coefficients can be interpreted as indicating a positive (negative) association between regions with greater white matter intensity than gray matter intensity and BOLDVAR. Focusing on trends in each lobe in Figure 10 (a), the estimated coefficient function shows a mixture of associations, with positive coefficients observed in the occipital lobe, negative coefficients observed in the limbic, insula, and parietal lobes, and a mixture of positive and negative coefficients in the temporal and frontal lobes. Estimated effects range from -0.3 to 0.3 , indicating that within each ROI a SD increase in GWMIC is associated with generally less than a 0.3 SD shift in the outcome $\log(\text{BOLDVAR})$ reflecting a modest effect size. Figure 10(b) shows the length of the 95% credible intervals for the estimated coefficient function, offering a measure of uncertainty—longer intervals reflect greater uncertainty, while shorter intervals indicate less uncertainty. When the posterior 95% credible interval contains zero, the interval length is marked with back stripes in the Figure10(b). While 95% credible intervals for ROI-effects include zero within each lobe, the greatest concentration of striping is observed in the frontal and occipital lobes suggesting this is where our XAI model is not certain of an association between GWMIC and the outcome. Situating these results in relation to prior research, Zuo et al. [2010] found that gray matter in the brain displays higher

ALFF than white matter, though these results focus on gray and white matter parcellations of the brain as opposed to cortical contrasts analyzed here. In fact, the relationship between BOLDVAR and GWMIC is essentially unexplored in adolescent children and these findings suggest a mixture of associations both within and across brain lobes when controlling for the contributions of CT and multi-task coactivation.

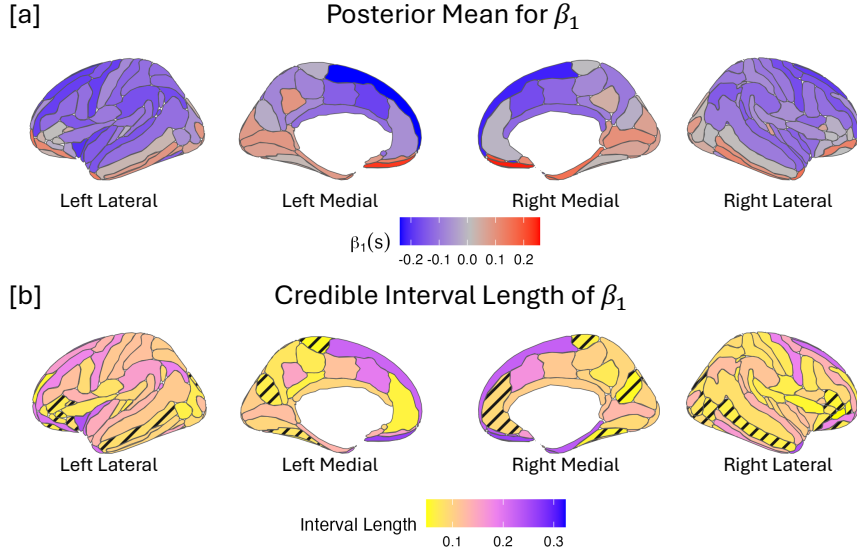


Figure 10: Lateral and medial cross sections of the posterior **(a)** mean and **(b)** 95% credible interval length for the spatially varying coefficient function $\beta_1(\mathbf{s}_{v,j})$ capturing effects of GWMIC. When the posterior 95% credible interval contains zero, the interval length is marked with back stripes in the figure as indication of uncertainty of any association.

Figure 11 displays lateral and medial cross sections of the posterior (a) mean and (b) 95% credible interval length for the spatially varying coefficient function $\beta_2(\mathbf{s}_{v,j})$ capturing effects of CT. Focusing on trends in each lobe in Figure 11 (a), the estimated coefficient function is negative across the brain, with the strongest associations observed in the frontal and limbic lobes and the weakest associations observed in the occipital lobe. Estimated effects range from -0.3 to 0.0 , indicating that within each ROI a SD increase in CT is associated with up to a 0.3 SD decrease in the outcome $\log(\text{BOLDVAR})$ reflecting a modest effect size. Figure 11(b), displays the 95% credible interval length for the estimated coefficient function and are interpreted as described above. Generally, 95% credible intervals for ROI-effects exclude zero with the exception of a few ROIs in the frontal lobe suggesting our XAI model is relatively certain of the associ-

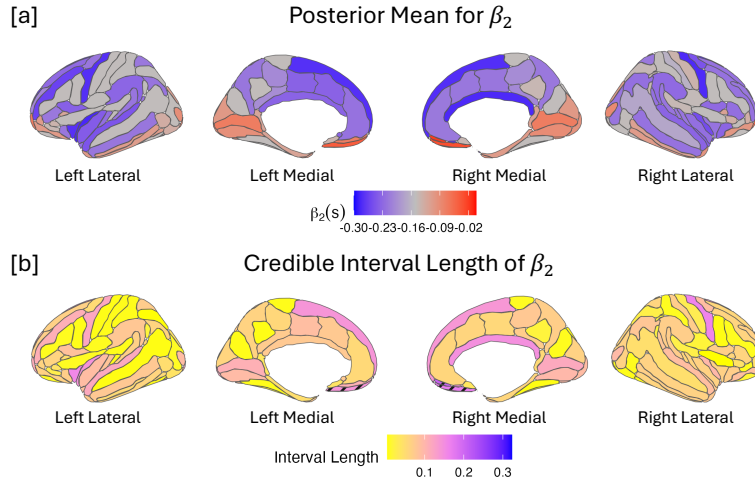


Figure 11: Lateral and medial cross sections of the posterior **(a)** mean and **(b)** 95% credible interval length for the spatially varying coefficient function $\beta_2(\mathbf{s}_{v,j})$ capturing effects of CT. When the posterior 95% credible interval contains zero, the interval length is marked with back stripes in the figure as indication of uncertainty of any association.

ation between CT and the outcome. There is essentially no prior research on the relationship between BOLDVAR and CT in adolescent children and these results suggest a near uniform negative association throughout the brain that varies in magnitude from no effect to modest effects when controlling for the contributions of GWMIC and multi-task coactivation. Table

Table 4: Predictive inference results for real data application from different methods. For all methods, prediction accuracy, 95% HPD interval, prediction coverage, and computing time (min) are reported in the table.

		XAI	BART	BIRD-GP	GLM
Prediction (Training)	RMSE	1.0012	0.9808	1.4347	0.9776
Prediction (Test)	RMSPE	1.0008	0.9793	2.0345	0.9903
	Coverage	0.9487	0.0801	0.9293	-
	Intervals	6.2941	0.1940	7.2426	-
Time (min)		38.1203	160.7703	126.0806	0.2515

4 displays the predictive inference and computational time for our technique compared to the listed competitors. In both training (RMSE) and testing (RMSPE), all models produce similar errors in testing and training with approximate equivalence across models with the exception of BIRD-GP which performs considerably worse at both testing and training. In terms of our ABCD data, this suggests that our proposed XAI which assumes an additive decomposition of

structural and network predictor effects (with the added assumption of linearity for effects of the structural predictors) fits our outcome image as well as the competitor model BART which allows interactions between image modalities to form predictions. In comparison to the the GLM, our proposed model performs similarly but provides predictive inference whereas GLM does not. Among the techniques that provide posterior predictive inference, our proposed XAI model provides nominal coverage followed by BIRD-GP with near nominal coverage and BART with severe under coverage. In terms of credible interval length, BART provides the shortest intervals, explaining its poor coverage, while XAI provides substantially narrower intervals than BIRD-GP despite providing superior coverage. In terms of computation, while the GLM procedure naturally has the fastest computation time, the XAI procedure takes approximately four times less than than other competitors that offer posterior predictive inference. In conclusion, our proposed model provides equivalent point prediction to its competitors while yielding superior predictive uncertainties and much faster computation which are of critical importance when dealing with large neuroimaging data sets.

7 Conclusion

This article proposes a predictive modeling framework for estimating spatially-indexed brain activation maps from task-based fMRI (t-fMRI), using spatially-resolved cortical metrics derived from structural MRI (s-MRI) and brain connectivity networks obtained from resting-state fMRI (rs-fMRI). The framework leverages deep neural networks to model complex nonlinear relationships between the input spatial and network-valued images and the spatial output image. It enables accurate estimation of the effect of each input image on the predicted activation map while providing crucial uncertainty quantification within DNN—both for prediction and for effect estimation—through a Monte Carlo (MC) dropout strategy. The proposed explainable AI (XAI) approach demonstrates superior predictive performance compared to widely-used nonlinear regression methods and existing deep learning models for image-on-image regression. Additionally, the model scales linearly with the sample size and the number of brain regions, ensuring computational efficiency in high-resolution and large-scale neuroimaging studies.

While this article assumes a common relationship between the activation map, cortical metrics, and brain connectivity network across all subjects, an important direction for future work is to investigate how these relationships vary across individuals. This motivates the development of model-based clustering strategies, wherein the proposed XAI framework is fitted within each identified cluster. This extension is the focus of our ongoing research.

8 Acknowledgements

Rajarshi Guhaniyogi acknowledges funding from National Science Foundation Grant DMS-2220840 and DMS-2210672. Aaron Scheffler acknowledges funding from National Science Foundation Grant DMS-2210206. Aaron Scheffler and Rajarshi Guhaniyogi acknowledge funding from the National Institute Of Neurological Disorders And Stroke of the National Institutes of Health under Award Number R01NS131604.

9 ABCD Data Acknowledgement

Data used in the preparation of this article were obtained from the Adolescent Brain Cognitive DevelopmentSM (ABCD) Study (<https://abcdstudy.org>), held in the NIMH Data Archive (NDA). This is a multisite, longitudinal study designed to recruit more than 10,000 children age 9-10 and follow them over 10 years into early adulthood. The ABCD Study is supported by the National Institutes of Health and additional federal partners under award numbers U01DA041048, U01DA050989, U01DA051016, U01DA041022, U01DA051018, U01DA051037, U01DA050987, U01DA041174, U01DA041106, U01DA041117, U01DA041028, U01DA041134, U01DA050988, U01DA051039, U01DA041156, U01DA041025, U01DA041120, U01DA051038, U01DA041148, U01DA041093, U01DA041089, U24DA041123, U24DA041147. A full list of supporters is available at <https://abcdstudy.org/federal-partners.html>. A listing of participating sites and a complete listing of the study investigators can be found at https://abcdstudy.org/consortium_members. ABCD consortium investigators designed and implemented the study and/or provided data but did not necessarily participate in the analysis or writing of this report. This manuscript reflects the views of the authors and may

not reflect the opinions or views of the NIH or ABCD consortium investigators. The ABCD data repository grows and changes over time. The ABCD data used in this report came from doi: 10.15154/8873-zj65.

References

Seyed Amir Hossein Batouli and Minoos Sisakhti. Some points to consider in a task-based fmri study: A guideline for beginners. *Frontiers in Biomedical Technologies*, 2020.

Ingwer Borg and Patrick JF Groenen. *Modern multidimensional scaling: Theory and applications*. Springer Science & Business Media, 2005.

B J Casey, Tariq Cannonier, May I Conley, Alexandra O Cohen, Deanna M Barch, and et al. The adolescent brain cognitive development (ABCD) study: Imaging acquisition across 21 sites. *Dev. Cogn. Neurosci.*, 32:43–54, August 2018.

Hugh A. Chipman, Edward I. George, and Robert E. McCulloch. Bart: Bayesian additive regression trees. *The Annals of Applied Statistics*, 4(1):266 – 298, 2010. doi: 10.1214/09-AOAS285. URL <https://doi.org/10.1214/09-AOAS285>.

Michael W Cole, Takuya Ito, Danielle S Bassett, and Douglas H Schultz. Activity flow over resting-state networks shapes cognitive task activations. *Nat. Neurosci.*, 19(12):1718–1726, December 2016.

Christophe Destrieux, Bruce Fischl, Anders Dale, and Eric Halgren. Automatic parcellation of human cortical gyri and sulci using standard anatomical nomenclature. *Neuroimage*, 53(1): 1–15, October 2010.

Xin Di, Eun H Kim, Chu-Chung Huang, Shih-Jen Tsai, Ching-Po Lin, and et al. The influence of the amplitude of low-frequency fluctuations on resting-state functional connectivity. *Front. Hum. Neurosci.*, 7:118, April 2013.

Zening Fu, Yiheng Tu, Xin Di, Bharat B Biswal, Vince D Calhoun, and et al. Associations

- between functional connectivity dynamics and BOLD dynamics are heterogeneous across brain networks. *Front. Hum. Neurosci.*, 11:593, December 2017.
- Yarin Gal and Zoubin Ghahramani. Dropout as a Bayesian approximation: Representing model uncertainty in deep learning. In *International Conference on Machine Learning*, pages 1050–1059. PMLR, 2016.
- Alan E Gelfand, Hyon-Jung Kim, CF Sirmans, and Sudipto Banerjee. Spatial modeling with spatially varying coefficient processes. *Journal of the American Statistical Association*, 98(462):387–396, 2003.
- Sharmistha Guha and Abel Rodriguez. Bayesian regression with undirected network predictors with an application to brain connectome data. *Journal of the American Statistical Association*, 116(534):581–593, 2021.
- Rajarshi Guhaniyogi and David B Dunson. Compressed gaussian process for manifold regression. *Journal of Machine Learning Research*, 17(69):1–26, 2016.
- Rajarshi Guhaniyogi, Cheng Li, Terrance D Savitsky, and Sanvesh Srivastava. Distributed bayesian varying coefficient modeling using a gaussian process prior. *Journal of machine learning research*, 23(84):1–59, 2022.
- Rajarshi Guhaniyogi, Cheng Li, Terrance Savitsky, and Sanvesh Srivastava. Distributed bayesian inference in massive spatial data. *Statistical science*, 38(2):262–284, 2023.
- Rajarshi Guhaniyogi, Laura Baracaldo, and Sudipto Banerjee. Bayesian data sketching for varying coefficient regression models. 2024.
- Donald J Hagler, Jr, Seann Hatton, M Daniela Cornejo, Carolina Makowski, Damien A Fair, and et al. Image processing and analysis methods for the adolescent brain cognitive development study. *Neuroimage*, 202:116091, nov 2019.
- Trevor Hastie and Robert Tibshirani. Varying-coefficient models. *Journal of the Royal Statistical Society Series B: Statistical Methodology*, 55(4):757–779, 1993.

- Lisa Herzog, Elvis Murina, Oliver Dürr, Susanne Wegener, and Beate Sick. Integrating uncertainty in deep neural networks for mri based stroke analysis. *Medical image analysis*, 65: 101790, 2020.
- He Huang, Philip S Yu, and Changhu Wang. An introduction to image synthesis with generative adversarial nets. *arXiv preprint arXiv:1803.04469*, 2018.
- Phillip Isola, Jun-Yan Zhu, Tinghui Zhou, and Alexei A Efros. Image-to-image translation with conditional adversarial networks. In *Proceedings of the IEEE conference on computer vision and pattern recognition*, pages 1125–1134, 2017.
- Yeseul Jeon, Won Chang, Seonghyun Jeong, Sanghoon Han, and Jaewoo Park. A bayesian convolutional neural network-based generalized linear model. *Biometrics*, 80(2), 2024.
- Charlie Kirkwood, Theo Economou, Nicolas Pugeault, and Henry Odbert. Bayesian deep learning for spatial interpolation in the presence of auxiliary information. *Mathematical Geosciences*, 54(3):507–531, 2022.
- Kexuan Li, Jun Zhu, Anthony R Ives, Volker C Radeloff, and Fangfang Wang. Semiparametric regression for spatial data via deep learning. *Spatial Statistics*, 57:100777, 2023.
- Guanxiong Luo, Na Zhao, Wenhao Jiang, Edward S Hui, and Peng Cao. Mri reconstruction using deep bayesian estimation. *Magnetic resonance in medicine*, 84(4):2246–2261, 2020.
- H Lv, Z Wang, E Tong, L M Williams, G Zaharchuk, and et al. Resting-State functional MRI: Everything that nonexperts have always wanted to know. *AJNR Am. J. Neuroradiol.*, 39(8): 1390–1399, August 2018.
- Guoxuan Ma, Bangyao Zhao, Hasan Abu-Amara, and Jian Kang. Bayesian image-on-image regression via deep kernel learning based gaussian processes. *arXiv preprint arXiv:2311.05649*, 2023.
- Jorge Mateu and Abdollah Jalilian. Spatial point processes and neural networks: A convenient couple. *Spatial Statistics*, 50:100644, 2022.

- Jeffrey S Morris. Functional regression. *Annual Review of Statistics and Its Application*, 2(1): 321–359, 2015.
- Eric W Prince, Debashis Ghosh, Carsten Görg, and Todd C Hankinson. Uncertainty-aware deep learning classification of adamantinomatous craniopharyngioma from preoperative mri. *Diagnostics*, 13(6):1132, 2023.
- Muhammad Imran Razzak, Saeeda Naz, and Ahmad Zaib. Deep learning for medical image processing: Overview, challenges and the future. *Classification in BioApps: Automation of decision making*, pages 323–350, 2018.
- Philip T Reiss, Jeff Goldsmith, Han Lin Shang, and R Todd Ogden. Methods for scalar-on-function regression. *International Statistical Review*, 85(2):228–249, 2017.
- Venkataraman Santhanam, Vlad I Morariu, and Larry S Davis. Generalized deep image to image regression. In *Proceedings of the IEEE conference on computer vision and pattern recognition*, pages 5609–5619, 2017.
- João Ricardo Sato, Claudinei Eduardo Biazoli Jr, Luciana Monteiro Moura, Nicolas Crossley, André Zugman, and et al. Association between fractional amplitude of Low-Frequency spontaneous fluctuation and degree centrality in children and adolescents. *Brain Connect.*, 9(5): 379–387, June 2019.
- Jintao Sheng, Liang Zhang, Junjiao Feng, Jing Liu, Anqi Li, and et al. The coupling of BOLD signal variability and degree centrality underlies cognitive functions and psychiatric diseases. *Neuroimage*, 237:118187, August 2021.
- Rodney Sparapani, Charles Spanbauer, and Robert McCulloch. Nonparametric machine learning and efficient computation with bayesian additive regression trees: The bart r package. *Journal of Statistical Software*, 97:1–66, 2021.
- Jing Sui, Tülay Adalı, Qingbao Yu, Jiayu Chen, and Vince D Calhoun. A review of multivariate

- methods for multimodal fusion of brain imaging data. *J. Neurosci. Methods*, 204(1):68–81, February 2012.
- D Tomasi, E Shokri-Kojori, and N D Volkow. Temporal changes in local functional connectivity density reflect the temporal variability of the amplitude of low frequency fluctuations in gray matter. *PLoS One*, 11(4):e0154407, April 2016.
- Dardo Tomasi and Nora D Volkow. Association between brain activation and functional connectivity. *Cereb. Cortex*, 29(5):1984–1996, May 2019.
- Masayuki Tsuneki. Deep learning models in medical image analysis. *Journal of Oral Biosciences*, 64(3):312–320, 2022.
- Hongye Wang, Amirhossein Ghaderi, Xiangyu Long, Jess E Reynolds, Catherine Lebel, and Andrea B Protzner. The longitudinal relationship between BOLD signal variability changes and white matter maturation during early childhood. *Neuroimage*, 242:118448, November 2021.
- Christopher G. Watson. braingraph: Graph theory analysis of brain mri data, 2020. URL <https://CRAN.R-project.org/package=brainGraph>.
- Christopher K Wikle and Andrew Zammit-Mangion. Statistical deep learning for spatial and spatiotemporal data. *Annual Review of Statistics and Its Application*, 10(1):247–270, 2023.
- Fengdan Ye, Robert Kohler, Bianca Serio, Sarah Lichenstein, and Sarah W Yip. Task-based co-activation patterns reliably predict resting state canonical network engagement during development. *Dev. Cogn. Neurosci.*, 58(101160), December 2022.
- Andrew Zammit-Mangion, Michael D Kaminski, Ba-Hien Tran, Maurizio Filippone, and Noel Cressie. Spatial bayesian neural networks. *arXiv preprint arXiv:2311.09491*, 2023.
- Daiwei Zhang, Lexin Li, Chandra Sripada, and Jian Kang. Image response regression via deep neural networks. *Journal of the Royal Statistical Society Series B: Statistical Methodology*, 85(5):1589–1614, 2023a.

Jianfeng Zhang, Dong-Qiang Liu, Shufang Qian, Xiujuan Qu, Peiwen Zhang, and et al. The neural correlates of amplitude of low-frequency fluctuation: a multimodal resting-state MEG and fMRI-EEG study. *Cereb. Cortex*, 33(4):1119–1129, February 2023b.

Ke Zou, Zhihao Chen, Xuedong Yuan, Xiaojing Shen, Meng Wang, and et al. A review of uncertainty estimation and its application in medical imaging. *Meta-Radiology*, page 100003, 2023.

Xi-Nian Zuo, Adriana Di Martino, Clare Kelly, Zarrar E Shehzad, Dylan G Gee, and et al. The oscillating brain: complex and reliable. *Neuroimage*, 49(2):1432–1445, January 2010.